Probing new physics of cubic Higgs boson interaction via Higgs pair production at hadron colliders

Hong-Jian He, Jing Ren, and Weiming Yao

Phys. Rev. D **93**, 015003 — Published 7 January 2016

DOI: 10.1103/PhysRevD.93.015003

Probing New Physics of Cubic Higgs Interaction via Higgs Pair Production at Hadron Colliders

Hong-Jian He [a*], Jing Ren [b†], Weiming Yao [c‡]

[a] Institute of Modern Physics and Center for High Energy Physics, Tsinghua University, Beijing 100084, China; Harvard University, 1 Oxford Street, Cambridge, MA 02138, USA; Institute for Advanced Study, Princeton, NJ 08540, USA

[b] Department of Physics, University of Toronto, Toronto ON Canada M5S1A7

[c] Lawrence Berkeley National Laboratory, Berkeley CA 94720, USA

Abstract

Despite the discovery of a Higgs boson $h(125\,\mathrm{GeV})$ at the LHC Run-1, its self-interaction has fully evaded direct experimental probe so far. Such self-interaction is vital for electroweak symmetry breaking, vacuum stability and electroweak phase transition. It is a most likely place to encode new physics beyond the standard model. We parametrize such new physics by model-independent dimension-6 effective operators, and study their tests via Higgs pair production at hadron colliders. We analyze three major dihiggs production channels at parton level, and compare the parameter-dependence of total cross sections and kinematic distributions at the LHC (14TeV) and pp(100TeV) hadron collider. We further perform full simulations for the dihiggs production channel $gg \to hh \to b\bar{b}\gamma\gamma$ and its backgrounds at the pp (100TeV) hadron collider. We construct four kinds of benchmark points, and study the sensitivities to probing different regions of the parameter space of cubic Higgs interactions. We find that for one-parameter analysis and with a $3\,\mathrm{ab}^{-1}$ $(30\,\mathrm{ab}^{-1})$ integrated luminosity, the $gg \to hh \to b\bar{b}\gamma\gamma$ channel can measure the SM cubic Higgs coupling and the derivative cubic Higgs coupling to an accuracy of about 13% (4.2%) and 5% (1.6%), respectively.

PACS numbers: 12.60.Fr, 12.60.-i, 14.80.Bn [arXiv:1506.03302]

*Email: hjhe@tsinghua.edu.cn
†Email: jren@physics.utoronto.ca
‡Email: wmyao@lbl.gov

1. Introduction

The LHC discovery of the light Higgs boson $h\,(125\,\text{GeV})$ [1] has become a historical turning point of particle physics. The standard model (SM) [2] could provide such a Higgs boson [3], which joins three types of fundamental interactions: (i) the gauge interactions mediated by spin-1 weak gauge bosons (W, Z); (ii) the Yukawa interactions with fermions mediated by the spin-0 Higgs boson h; (iii) and the cubic and quartic Higgs self-interactions h^3 and h^4. But the type-(ii) and type-(iii) Higgs interactions are largely untested so far, which provide the most likely place to encode new physics beyond the SM. The current ATLAS and CMS measurements [4] find the Higgs boson $h\,(125\,\text{GeV})$ to appear SM-like, but only have weak sensitivities to $h\tau\bar{\tau}$ and $hb\bar{b}$ Yukawa couplings, while even the LHC run-2 could not sensitively probe most of other Yukawa couplings via direct detection [5]. Furthermore, the LHC has little sensitivity to probing the type-(iii) Higgs self-interactions. It was shown that the high luminosity LHC $(14\,\text{TeV})$ with an integrated luminosity of $3\,\text{ab}^{-1}$ could probe the h^3 coupling to about 50% accuracy [6, 7], and the improved analysis could reach a sensitivity about $30\% - 20\%$ [8]. With the current measurements of Higgs and top quark masses, the SM Higgs vacuum becomes unstable around 10^{9-11}GeV [9] and is very sensitive to new physics [10]. So new physics is expected to enter the Higgs potential and modify its self-interactions well below Planck scale [9, 10]. The Higgs self-interactions are vital for the spontaneous electroweak symmetry breaking [2], the electroweak phase transition [11], and the Higgs inflation [12]. Hence, it is important to probe Higgs self-interactions with precision and pin down the associated new physics deviations from the SM.

The SM Higgs sector is described by the gauge-invariant renormalizable Higgs potential,

$$V = -\mu^2 H^\dagger H + \lambda (H^\dagger H)^2, \tag{1.1}$$

where $H = (\pi^+, \frac{1}{\sqrt{2}}(v + h + \mathrm{i}\pi^0))^T$ is the Higgs doublet and $v \simeq 246\,\text{GeV}$ denotes the vacuum expectation value (VEV). Thus, the Higgs self-interactions take the form,

$$V_{\text{int}} \;=\; \frac{\lambda_3}{3!} h^3 + \frac{\lambda_4}{4!} h^4\,, \tag{1.2}$$

where at tree-level we have the cubic and quartic couplings of the SM Higgs boson, $\lambda_3 = 6\lambda v = 3M_h^2/v$ and $\lambda_4 = 6\lambda = 3M_h^2/v^2$. Hence, given the observed Higgs mass $M_h \simeq 125\,\text{GeV}$ [1], the Higgs self-couplings are completely determined in the SM. One could naively make a shift of Higgs coupling within the SM Higgs potential (1.1), $\lambda \to \lambda' = \lambda + \delta\lambda\,,$ but it causes no observable effect, because this just redefines the *renormalizable* Higgs coupling as λ' no matter what value $\delta\lambda$ would take.

The nontrivial modification of Higgs couplings could only arise from higher dimensional effective operators whose effects cannot be absorbed into the dimension-4 SM Lagrangian.

Given that the SM Lagrangian already contains all possible gauge-invariant and renormalizable operators up to dimension-4 and no new physics is found yet, the possible leading new physics deviations from the SM can be generally parametrized by gauge-invariant dimension-6 effective operators in a model-independent way [13]. Since the Higgs potential acts as the core of spontaneous electroweak symmetry breaking and has escaped from direct measurement so far, it stands out as a most likely place to encode new physics beyond the SM. Such new physics will certainly modify the Higgs self-interactions (1.2), via dimension-6 operators, which may not only shift the Higgs self-coupling itself [due to the operator $(H^\dagger H)^3$], but also modify the structure of Higgs self-interactions (due to the dimension-6 derivative operators). To sensitively probe such new physics in the cubic Higgs self-coupling, it is important to study dihiggs production at high energy hardon colliders [14, 15].[1]

For hadron colliders, the main dihiggs production channels include gluon fusion production, vector boson fusion (VBF) production, and top-pair associated production. Over a wide energy range, the total cross section of dihiggs production via gluon fusions is almost 10 times larger than the other channels [15][17]. Hence, it provides the dominant dihiggs production. The decay mode $hh \to b\bar{b}\gamma\gamma$ has much cleaner background than others, so it has attracted efforts from both theoretical and experimental sides [6][18][19] for studying the potential of the high luminosity LHC (14TeV) and the future pp(100TeV) collider. Other dihiggs decay modes with larger signal rates are also explored, such as $hh \to b\bar{b}\tau\tau$, $hh \to b\bar{b}WW^* \to b\bar{b}2\ell 2\nu$, and $hh \to b\bar{b}b\bar{b}$, etc [20]. Due to large backgrounds in these channels, more elaborated strategies like boosted kinematics are needed. Another decay mode $hh \to WW^*WW^* \to 3\ell 3\nu jj$ was considered with the use of m_{T2} observable [21]. Some rare final states were also explored for pp(100TeV) collider [22]. In addition, two more production channels have received recent attentions. The top-pair associated production $pp \to t\bar{t}hh$ turns out to be complementary to gluon fusion $gg \to hh$ with $hh \to b\bar{b}b\bar{b}$ final states [23]. The VBF production channel $pp \to hhjj$ receives a large contribution from gluon fusion production in the signal region, which makes the VBF contribution almost negligible [24]. Most previous studies for the dihiggs production focused on the SM Higgs potential. There are recent analyses studying the contributions of dimension-6 operators to $gg \to hh$ with $hh \to b\bar{b}\gamma\gamma$ [25] and $hh \to b\bar{b}\tau\tau$ [26]. It was noted that certain new operators can modify kinematic distributions of the final states as well as total cross section. For an operator that induces $t\bar{t}hh$ coupling, the kinematics could be useful to increase the sensitivity [27, 28]. In general, including these operators with associated new coefficients will enlarge the parameter space of new physics, and thus make the probe of each individual parameter in the cubic Higgs interaction harder. Certain simplifications are needed to reduce the large parameter

[1] Measuring Higgs quartic coupling would be even more challenging in the foreseeable future [16].

space.

In this work, we will systematically analyze the new physics contributions of dimension-6 operators to the dihiggs productions. For good physics reasons, we will focus on two rather unique bosonic dimension-6 operators which contribute to the cubic Higgs coupling and build a 2-dimensional (2d) parameter space. In particular, we will inspect the new operator that induces derivative cubic Higgs coupling, and thus has enhanced contributions to high energy processes. We will derive nontrivial perturbative unitarity constraints on these dimension-6 operators. Then, we study the dihiggs production via three major channels for probing cubic Higgs couplings. For this, we will perform a parton level analysis at the LHC (14TeV) and pp (100TeV) collider. Finally, we present a full analysis (including Delphes 3 fast detector simulations) for the dihiggs production $gg \to hh$ with $hh \to b\bar{b}\gamma\gamma$ at the pp (100TeV) collider. From this we study the probe of new physics scales associated with the dimension-6 operators. We also find nontrivial interference between different operators, which can be probed by using relevant kinematic distributions.

This paper is organized as follows. In section 2, we discuss the dimension-6 operators relevant to Higgs self-interactions, and identify the unique operators (2.16) which spans a 2d parameter space. We also motivate these operators by nonminimal Higgs-gravity interaction. We further study the perturbative unitarity constraints on the cutoff scales associated with dimension-6 operators. In section 3, we analyze three major dihiggs production channels at parton level and compare the parameter-dependence of total cross sections and kinematic distributions. In section 4, we perform full simulations for $gg \to hh \to b\bar{b}\gamma\gamma$ at the 100 TeV hadron collider, and study the sensitivity to the 2d parameter space for three benchmarks. We conclude in section 5. Finally, Appendix A discusses the redundancy of dimension-6 operators, and Appendix B summarizes the loop functions of triangle and box diagrams for the analyses of sections 3–4.

2. New Higgs Self-Interactions from Dimension-6 Operators

2.1. Identifying Relevant Dimension-6 Operators

The SM Lagrangian is a fairly good effective theory up to gauge-invariant renormalizable operators of dimension-4. The possible leading new physics deviations are generally parametrized via dimension-6

effective operators,[2]

$$\mathcal{L}_{\rm eff} \;=\; \sum_n \frac{f_n}{\Lambda^2}\mathcal{O}_n\,, \tag{2.3}$$

where Λ characterizes the cutoff scale, and the dimensionless coupling f_n is expected to be around $O(0.1-1)$ for each given operator (unless suppressed by extra symmetry). The LHC Run-1 data [4] have constrained the 125 GeV Higgs boson to be fairly SM-like and found no new light particle beyond the SM. Hence, it is well-motivated to use the standard effective theory formulation of possible new physics effects via dimension-6 operators [13], and assume that no other light field exists below its cutoff scale. The full set of gauge-invariant dimension-6 operators that modify Higgs self-interactions includes [30],

$$\begin{aligned}
&\mathcal{O}_{\Phi,1} = (D^\mu H)^\dagger H H^\dagger (D_\mu H)\,, \qquad && \mathcal{O}_{\Phi,2} = \frac{1}{2}\partial^\mu (H^\dagger H)\partial_\mu (H^\dagger H)\,,\\
&\mathcal{O}_{\Phi,3} = \frac{1}{3}(H^\dagger H)^3, && \mathcal{O}_{\Phi,4} = (D^\mu H)^\dagger (D_\mu H)(H^\dagger H)\,.
\end{aligned} \tag{2.4}$$

Among all four operators, $\mathcal{O}_{\Phi,2}$ and $\mathcal{O}_{\Phi,3}$ modify scalar sectors only, while $\mathcal{O}_{\Phi,1}$ and $\mathcal{O}_{\Phi,4}$ also contribute to gauge boson masses and couplings. The operator $\mathcal{O}_{\Phi,1}$ contributes to the mass m_Z, but not to m_W. Thus, it violates the custodial symmetry and is severely constrained by the electroweak precision parameter T. For collider searches, it is safe to neglect the effects of $\mathcal{O}_{\Phi,1}$ [31]. With the equation of motion (EOM), there is redundancy among dimension-6 operators. As explained in Appendix A, the subset operators ($\mathcal{O}_{\Phi,2}$, $\mathcal{O}_{\Phi,3}$, $\mathcal{O}_{\Phi,4}$) in (2.4) are not independent. Including the SM Yukawa interactions, another type of dimension-6 operators $\mathcal{O}_{\Phi,f}$ become relevant,

$$\mathcal{O}_{\Phi,f} \;=\; (H^\dagger H)\,\overline{L} H f_R + \text{h.c.}, \tag{2.5}$$

where $L = (f_L^u,\, f_L^d)^T$ denotes the $SU(2)_L$ doublet, and f_R the $SU(2)_L$ singlet. Among all operators mentioned above, one operator can be eliminated via EOM. We choose to drop $\mathcal{O}_{\Phi,4}$ hereafter. Thus, we have two rather unique bosonic dimension-6 operators ($\mathcal{O}_{\Phi,2}$, $\mathcal{O}_{\Phi,3}$) relevant to the present study of Higgs self-couplings.

Next, we inspect the contributions of ($\mathcal{O}_{\Phi,2}$, $\mathcal{O}_{\Phi,3}$, $\mathcal{O}_{\Phi,f}$) to the Higgs self-couplings, as well as the Higgs-gauge and Higgs-fermion couplings. For later convenience, we define a dimensionless coefficient x_j and an effective cutoff scale $\tilde{\Lambda}_j$ for each operator in (2.4)-(2.5),

$$x_j \;\equiv\; \frac{f_{\Phi,j} v^2}{\Lambda^2} \;\equiv\; \text{sign}(f_{\Phi,j})\frac{v^2}{\tilde{\Lambda}_j^2}\,, \qquad\qquad \tilde{\Lambda}_j \;\equiv\; \frac{\Lambda}{\sqrt{|f_{\Phi,j}|}}\,. \tag{2.6}$$

[2] If the light neutrinos turn out to be Majorana fermions, there is a unique dimension-5 effective operator [29], $(f^\nu_{ij}/\Lambda_5) H^\alpha H^\beta L_i^{\alpha' T} \hat{C} L_j^{\beta'} \epsilon_{\alpha\alpha'}\epsilon_{\beta\beta'}$, which provides Majorana neutrino masses and violates lepton number by two units. Here $\hat{C} = i\gamma^2\gamma^0$ is the charge-conjugation operator, (i,j) are flavor indices of left-handed lepton doublet, and $(\alpha,\alpha',\beta,\beta')$ are indices of SU(2) doublets. This dimension-5 operator is irrelevant to our current study of the Higgs self-interactions.

Since $\mathcal{O}_{\Phi,3}$ is a non-derivative operator, it only affects Higgs mass and self-couplings. In particular, it modifies the relation between the observed Higgs mass and cubic Higgs coupling. The derivative operator $\mathcal{O}_{\Phi,2}$ induces the following term for Higgs field,

$$\mathcal{O}_{\Phi,2} \;\to\; \frac{x_2}{2v^2}(h+v)^2\partial^\mu h\partial_\mu h\,, \tag{2.7}$$

with x_2 defined in (2.6). This modifies the Higgs kinetic term as,

$$\mathcal{L}_{\rm kin} \;=\; \frac{1}{2}\,(1+x_2)\,\partial^\mu h\partial_\mu h\,. \tag{2.8}$$

Thus, we can define the canonical Higgs field via rescaling $h\to\zeta h$, with the factor,

$$\zeta \;\equiv\; (1+x_2)^{-\frac{1}{2}}\,. \tag{2.9}$$

This induces a universal modification to all Higgs couplings with SM particles. After the normalization, Eq. (2.7) also generates a derivative cubic Higgs interaction, $\frac{1}{v}x_2\zeta^3 h\partial^\mu h\partial_\mu h$. In contrast to the SM cubic Higgs coupling, this new derivative interaction vertex will be enhanced by the center of mass energy in high energy processes, and thus may have distinctive kinematic feature. The modified cubic Higgs coupling is

$$\begin{aligned} h-h-h\colon\qquad & -\mathrm{i}\frac{3M_h^2}{v}\zeta\left(1-x_3\zeta^2\frac{2v^2}{3M_h^2}\right)+\mathrm{i}\frac{x_2}{v}\zeta^3\left(p_1^2+p_2^2+p_3^2\right)\\ & =-\mathrm{i}\frac{\zeta}{v}\left[\,3\,(1+\widehat{r})\,M_h^2-\widehat{x}\,\left(p_1^2+p_2^2+p_3^2\right)\,\right] \end{aligned} \tag{2.10}$$

In the above, M_h is the physical mass of the Higgs boson, which receives contributions from both the kinetic rescaling factor (2.9) and the dimension-6 operator $\mathcal{O}_{\Phi,3}$. So, we deduce the Higgs mass formula, $M_h^2 = M_{h0}^2[1-x_3/(2\lambda)]\zeta^2$, where $M_{h0}=\sqrt{2\lambda}\,v$ is the SM Higgs mass. We see that M_h depends on $\{\zeta, x_3\}$. For convenience, we replace $(x_2,\,x_3)$ by another two independent inputs $(\widehat{r},\,\widehat{x})$ which parametrize the modifications of cubic Higgs coupling with different kinematic properties,

$$\widehat{r} \;\equiv\; -x_3\,\zeta^2\frac{2v^2}{3M_h^2}\,,\qquad \widehat{x} \;\equiv\; x_2\,\zeta^2\,. \tag{2.11}$$

With $\widehat{x}$, the rescaling factor can be rewritten as $\zeta=(1-\widehat{x})^{1/2}$. We also note that the operators $(\mathcal{O}_{\Phi,2},\,\mathcal{O}_{\Phi,3})$ do not affect the W mass at tree-level, so the Higgs VEV is determined by the Fermi constant G_F as in the SM, $v=\left(\sqrt{2}G_F\right)^{-1/2}\simeq 246\,\mathrm{GeV}$. The modification to Higgs-gauge boson coupling only arises from rescaling the Higgs field,

$$V_\mu-V_\nu-h\colon\qquad \mathrm{i}\frac{2m_V^2}{v}\,\zeta\,\eta^{\mu\nu}, \tag{2.12a}$$

$$V_\mu-V_\nu-h-h\colon\qquad \mathrm{i}\frac{2m_V^2}{v^2}\,\zeta^2\eta^{\mu\nu}, \tag{2.12b}$$

where $V = W, Z$. In unitary gauge, the Higgs-fermion dimension-6 operator (2.5) generates following term,

$$\mathcal{O}_{\Phi,f} \;\to\; \frac{x_f}{2\sqrt{2}v^2}(v+h)^3 \bar{f} f \,. \tag{2.13}$$

This contributes to fermion mass, $m_f = \frac{v}{\sqrt{2}}\left(y_f^{\rm sm} - \frac{1}{2}x_f\right)$, where $y_f^{\rm sm}$ is the SM Yukawa coupling. At the same time, it modifies the $f - \bar{f} - h$ Yukawa coupling. Replacing $y_f^{\rm sm}$ by m_f, we deduce the following effective Yukawa coupling,

$$\bar{f} - f - h\colon \qquad -\mathrm{i}\frac{\zeta\, m_f}{v}\left(1 - \frac{x_f\, v}{\sqrt{2}\, m_f}\right) \tag{2.14}$$

This operator also induces a dimension-5 vertex $h^2 \bar{f} f$,

$$\bar{f} - f - h - h\colon \qquad \mathrm{i}\zeta^2 \frac{3x_f}{\sqrt{2}v} \,. \tag{2.15}$$

It contributes to the gluon fusion production $gg \to hh$ with triangle quark loop. Since top quark is most relevant in practice, it is natural to set $f = t$ for the present analysis.

The dimension-6 operators (2.4) and (2.5) are subject to constraints from measurements of single Higgs production at the LHC. The current data put the best bound on Higgs-gauge couplings (2.12a) [31]. For a future e^+e^- Higgs factory with 250 GeV collision energy, the sensitivity to $e^+e^- \to Zh$ cross section is expected to be $\delta\sigma/\sigma = \mathcal{O}(0.5\%)$ [32] with a $5\mathrm{ab}^{-1}$ integrated luminosity. This is a direct probe of the modification of Higgs-gauge couplings and thus constraints $|\widehat{x}|$ at 1% level [33]. The operator $\mathcal{O}_{\Phi,3}$ will contribute to the $e^+e^- \to Zh$ cross section via one-loop corrections [34]. From this, the sensitivity to $\lambda_3^{\rm sm}$ is estimated to be about 35% at the e^+e^- Higgs factory with a $5\mathrm{ab}^{-1}$ integrated luminosity. Besides, many other dimension-6 operators can contribute to the gauge boson kinetic terms and thus the wavefunction renormalization. This will further shift Higgs-gauge couplings, and make the constraint on individual operators much weakened. For top Yukawa coupling, the LHC run-2 has weak sensitivity to probing the deviations in (2.14). The precision of a high-luminosity LHC (HL-LHC) is expected to be around 10% [35].

Dihiggs production at high energy hadron colliders is an important way to measure the cubic Higgs coupling. The dimension-6 operators (2.4)-(2.5) contribute in different dihiggs production channels. For gluon fusion and top-pair associated production, three operators $\mathcal{O}_{\Phi,3}$, $\mathcal{O}_{\Phi,2}$ and $\mathcal{O}_{\Phi,t}$ are relevant. For the two operators that modify Higgs self-interactions, $\mathcal{O}_{\Phi,3}$ contributes to the SM cubic Higgs coupling by a simple shift (without affecting its Lorentz structure), and is commonly studied in the dihiggs production literature. On the other hand, $\mathcal{O}_{\Phi,2}$ induces derivative cubic Higgs coupling (2.10), and is rarely studied for dihiggs production. This operator contributes to the Higgs-gauge coupling via Higgs wavefunction renormalization and thus may receive constraint

from measuring single Higgs productions (via vector boson fusion or Higgs-gauge-boson associated production) at colliders. But, since other dimension-6 operators also contribute to the Higgs-gauge couplings with interferences and possible cancellations, there is no unique constraint on $\mathcal{O}_{\Phi,2}$.[3] Hence, it is important to directly probe the derivative cubic Higgs coupling induced by $\mathcal{O}_{\Phi,2}$ via dihiggs production, which has distinctive kinematic features from other non-derivative operators. For the present study, we will focus on the new physics contributions to the Higgs self-couplings in dihiggs production, and drop the fermionic operator $\mathcal{O}_{\Phi,t}$ (which was considered before [27][28] and is irrelevant to Higgs self-interactions)[4]. With these considerations, we define our parameter space by identifying the two rather unique bosonic dimension-6 operators,

$$\mathcal{O}_{\Phi,2} \,=\, \frac{1}{2}\partial^\mu(H^\dagger H)\partial_\mu(H^\dagger H)\,, \qquad \mathcal{O}_{\Phi,3} \,=\, \frac{1}{3}(H^\dagger H)^3. \tag{2.16}$$

In the following subsection 2.2, we will further motivate the operator $\mathcal{O}_{\Phi,2}$ from the Higgs-gravity interaction. Then, we derive generic perturbative unitarity bound on $\mathcal{O}_{\Phi,2}$ in Sec. 2.3.

2.2. Motivation from Higgs Gravitational Interaction

The world is apparently described by a joint effective theory of the SM and general relativity (GR) up to accessible energy scales so far. It is important to probe the interface between the SM and GR. With the LHC discovery of a light Higgs boson $h\,(125\text{GeV})$, there is a unique dimension-4 operator at this intersection, namely, the nonminimal interaction between the Higgs doublet H and the Ricci scalar-curvature $\mathcal{R}$ [36],

$$S_\xi \,=\, \int d^4x\,\sqrt{-g}\,\xi H^\dagger H\mathcal{R}\,, \tag{2.17}$$

where ξ is a dimensionless coupling. With the proper normalization of graviton propagator, it is clear that under perturbative expansion the coupling ξ is always associated with the suppression factor $1/M_{\rm Pl}^2$. Hence, $\xi \gg 1$ can be well consistent with perturbative calculation. The current LHC constraint on this coupling is actually rather weak, and ξ can be as large as $O(10^{15})$ [37][38]. Nontrivial constraints from perturbative unitarity were derived before [38]. The operator (2.17)

[3] One could expect other possible precision constraints on $\mathcal{O}_{\Phi,2}$ from such as the muon anomalous magnetic moment $g_\mu - 2$ at two-loop. Again, other new physics operators such as the dimension-5 Pauli term $F_{\mu\nu}\bar{\psi}\sigma^{\mu\nu}\psi$ (with ψ being muon field) can also contribute to $g_\mu - 2$ at tree-level and become dominant. Hence, there is no unique constraint on $\mathcal{O}_{\Phi,2}$ from $g_\mu - 2$ at two-loop.

[4] In principle, $\mathcal{O}_{\Phi,t}$ could be discriminated from $\mathcal{O}_{\Phi,2}$ and $\mathcal{O}_{\Phi,3}$ by further performing a combined analysis of three dihiggs production channels via gluon fusion, VBF production, and top-pair associated production. With these and the single Higgs production $gg \to h$, we may also discriminate another operator $G^{a\mu\nu}G^a_{\mu\nu}H^\dagger H$ (which does not modify the Higgs self-coupling). It is possible that some other dimension-6 operators may contribute to the backgrounds as well, but without any special cut or selection they are expected to be much smaller than the SM backgrounds (from the dimension-4 operators of the SM). For clarity of the current analysis, we assume that these additional operators are negligible.

has many physical applications such as the Higgs inflation [12], gravitational dark matter [39], and collider signatures [38]. Including this operator, we write the joint effective Lagrangian of the SM and GR,

$$S_{\rm J}=\int d^4x\,\sqrt{-g^{(J)}}\Big[\Big(\frac{1}{2}M^2+\xi H^\dagger H\Big)\,\mathcal{R}^{(J)}-\sum_j\frac{1}{4}F^a_{\mu\nu j}F_j^{\mu\nu a}+(D_\mu H)^\dagger(D^\mu H)-V(H)\Big], \tag{2.18}$$

where $\mathcal{R}^{(J)}$ is the Ricci scalar corresponding to the Jordan frame metric $g^{(J)}_{\mu\nu}$, and $F^a_{\mu\nu i}=(W^a_{\mu\nu},\,B^{\mu\nu})$ are gauge field strengths of the electroweak gauge group $SU(2)_L\otimes U(1)_Y$. In (2.18), we can readily include the SM fermionic Lagranian $\mathcal{L}_F$ as well, though it is not relevant to the discussion below. For practical applications, it is convenient to make a Weyl transformation for metric field, $g^{(E)}_{\mu\nu}=\Omega^2 g^{(J)}_{\mu\nu}$, with the factor

$$\Omega^2\;=\;\frac{M^2+2\xi H^\dagger H}{M_{\rm Pl}^2}\,. \tag{2.19}$$

After changing variable, we write down the action with new metric $g^{(E)}_{\mu\nu}$,

$$\begin{aligned}S_{\rm E}\;=\;&\int d^4x\,\sqrt{-g}\Big[\frac{1}{2}M_{\rm Pl}^2\mathcal{R}-\sum_j\frac{1}{4}F^a_{\mu\nu j}F_j^{\mu\nu a}+\frac{3\xi^2}{M_{\rm Pl}^2\Omega^4}\big(\partial_\mu(H^\dagger H)\big)^2\\&+\frac{1}{\Omega^2}(D_\mu H)^\dagger(D^\mu H)-\frac{1}{\Omega^4}V(H)\Big].\end{aligned} \tag{2.20}$$

For simplicity, we drop the superscript (E) for all geometric quantities associated with $g^{(E)}_{\mu\nu}$ here. Since the nonminimal interaction term is transformed away and the gravity sector becomes normal, the new metric is called Einstein frame. In this case, all effects of ξ appear in matter sector and are represented by a series of higher dimensional effective operators. Expanding these ξ-induced terms to leading order, we can deduce two relevant dimension-6 Higgs operators $\mathcal{O}_{\Phi,2}$ and $\mathcal{O}_{\Phi,3}$ from (2.20),

$$\frac{3}{\Lambda^2_{\xi1}}\big(\partial_\mu(H^\dagger H)\big)^2+\frac{4\lambda}{\Lambda^2_{\xi2}}\big(H^\dagger H\big)^3, \tag{2.21}$$

associated with two different cutoff scales,

$$\Lambda_{\xi1}=\frac{M_{\rm Pl}}{\xi},\quad \Lambda_{\xi2}=\frac{M_{\rm Pl}}{\sqrt{\xi}}. \tag{2.22}$$

Among dimension-6 operators in (2.4), $\Lambda_{\xi1}$ is related to $\mathcal{O}_{\Phi,2}$ with $f_{\Phi,2}/\Lambda^2=6/\Lambda^2_{\xi1}$, which is generated due to the third term of Eq. (2.20). Expanding the $1/\Omega$ factors in (2.20) will induce $(\mathcal{O}_{\Phi,3},\,\mathcal{O}_{\Phi,4},\,\mathcal{O}_{\Phi,f})$, with a cutoff characterized by $\Lambda_{\xi2}=M_{\rm Pl}/\sqrt{\xi}$. For the operator $\mathcal{O}_{\Phi,3}$, we have $f_{\Phi,3}/\Lambda^2=12/\Lambda^2_{\xi2}$. The other two operators $\mathcal{O}_{\Phi,4}$ and $\mathcal{O}_{\Phi,f}$ are induced from $1/\Omega$ expansion with the following coefficients,

$$-\frac{2}{\Lambda^2_{\xi2}}O_{\Phi,4}+\frac{4y_f}{\Lambda^2_{\xi2}}O_{\Phi,f}\,, \tag{2.23}$$

where y_f is the SM Yukawa coupling of the fermion f. The effective theory with such Higgs-gravity interactions can be viable for a wide range of ξ. To be relevant to collider physics, we need $\xi \gg 1$ [38][5], which implies $\Lambda_{\xi 1}^2 \ll \Lambda_{\xi 2}^2$. Hence, in this effective theory, the operator $\mathcal{O}_{\Phi,2}$ will give dominant contributions, while other operators $\mathcal{O}_{\Phi,3}$ and $(\mathcal{O}_{\Phi,4}, \mathcal{O}_{\Phi,f})$ are negligible.

2.3. Constraints from Perturbative Unitarity

In this subsection, we derive perturbative unitarity bound on the parameter space of dimension-6 operators defined in (2.16). We analyze the longitudinal weak boson scattering and top-Higgs scattering in high energy regime. We find that their scattering amplitudes are largely enhanced by E^2 and E^1 contributions from the derivative cubic Higgs couplings, and would eventually violate perturbative unitarity with the increase of scattering energy. This places an upper bound on the validity range of perturbation expansion of the effective theory, above which certain nonperturbative dynamics or new physics have to set in.[6] For the current analysis, we will derive perturbative unitarity bounds for both types of processes. Since the energy dependence of $gg \to hh$ amplitude is rather mild, it cannot place better bounds than the processes mentioned above, and thus needs no consideration here.

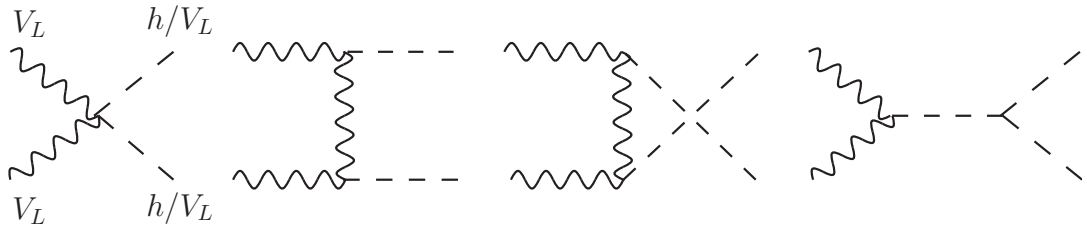

Figure 1: Longitudinal weak boson scattering processes, $V_L V_L \to hh\,(V_L V_L)$, where $V = W^{\pm}, Z^0$. The crossing channels also give gauge-Higgs boson scattering.

Fig. 1 depicts the longitudinal weak boson scattering $V_L V_L \to hh\,(V_L V_L)$ and the gauge-Higgs boson scattering in the crossing channels. The new physics of dimension-6 operators modifies the Higgs-gauge coupling and the Higgs self-couplings, which can induce nonzero $\mathcal{O}(E^2)$ enhancement in the scattering amplitudes [38]. Since dimension-6 operators are gauge-invariant, the longitudinal-Goldstone boson equivalence theorem (ET) [40] can be established [38]. Hence, the same E^2 en-

[5] As we clarified before [38], in this effective theory formulation, we do not concern any detail of the UV completion above the cutoff $\Lambda_{\xi 1,2}$. There are many well-motivated TeV scale quantum gravity theories on the market. For instance, extra dimensional models with compactification scale at $\Lambda_{\xi 1} = O(10\text{TeV})$ will reveal the Kaluza-Klein modes at energies above this scale, and other related UV dynamics may show up above this cutoff as well.

[6] Since the joint effective theory of SM+GR is nonrenormalizable and its UV completion is unknown, any naive partial resummation within this effective theory itself cannot give reliable unitarity restoration [38]. Hence, the perturbative unitarity bound is important for such nonrenormalizable effective theories.

hancement must show up in the corresponding Goldstone boson scattering amplitudes. To derive the optimal unitarity constraints on dimension-6 operators, we perform a coupled channel analysis of all electrically neutral channels for Goldstone boson and Higgs boson scatterings, with initial/final states $\{|\pi^+\pi^-\rangle\,,\,\frac{1}{\sqrt{2}}\,|\pi^0\pi^0\rangle\,,\,\frac{1}{\sqrt{2}}\,|hh\rangle\,,\,|\pi^0 h\rangle\}$. We compute the relevant leading scattering amplitudes at $\mathcal{O}(E^2)$,

$$\begin{aligned}
\mathcal{T}[\pi^+\pi^-\to\pi^+\pi^-] &= \widehat{x}\,\frac{(1+\cos\theta)E^2}{2v^2}, \\
\mathcal{T}[\pi^+\pi^-\to\pi^0\pi^0] &= \widehat{x}\,\frac{E^2}{v^2}\,, \\
\mathcal{T}[\pi^+\pi^-\to hh] &= \mathcal{T}[\pi^0\pi^0\to hh] \,=\, \widehat{x}\,(1-\widehat{x})\frac{E^2}{v^2}\,, \\
\mathcal{T}[\pi^0 h\to\pi^0 h] &= -\widehat{x}\,(1-\widehat{x})\frac{(1-\cos\theta)E^2}{2v^2}\,, \\
\mathcal{T}[\pi^0\pi^0\to\pi^0\pi^0] &= \mathcal{O}(E^0)\,, \qquad \mathcal{T}[hh\to hh] \,=\, \mathcal{O}(E^0)\,,
\end{aligned} \tag{2.24}$$

where E is the center-of-mass energy and θ denotes the scattering angle. With these, we compute the corresponding partial wave amplitudes,

$$a_\ell(E) \,=\, \frac{1}{32\pi}\int_{-1}^{1} d\cos\theta\, P_\ell(\cos\theta)\mathcal{T}(E,\theta)\,. \tag{2.25}$$

We perform a coupled channel analysis for the in/out states $\{|\pi^+\pi^-\rangle\,,\,\frac{1}{\sqrt{2}}\,|\pi^0\pi^0\rangle\,,\,\frac{1}{\sqrt{2}}\,|hh\rangle\,,\,|\pi^0 h\rangle\}$, Then, we can derive the following 4×4 matrix for the s-wave amplitudes at $\mathcal{O}(E^2)$,

$$a_0(E) \,=\, \frac{\widehat{x}\,E^2}{32\pi v^2}\begin{pmatrix} 1 & \sqrt{2} & \sqrt{2}(1-\widehat{x}) & 0 \\ \sqrt{2} & 0 & 1-\widehat{x} & 0 \\ \sqrt{2}(1-\widehat{x}) & 1-\widehat{x} & 0 & 0 \\ 0 & 0 & 0 & -(1-\widehat{x}) \end{pmatrix} \tag{2.26}$$

For a sizable $|1-\widehat{x}|$, the scattering amplitudes with Higgs in initial/final states have dominant contributions. We deduce the following eigenvalues,

$$a_0^{\rm diag}(E) \,=\, \frac{\widehat{x}\,E^2}{32\pi v^2}\,{\rm diag}\Big(1+\sqrt{1+3(1-\widehat{x})^2},\,1-\sqrt{1+3(1-\widehat{x})^2},\,-(1-\widehat{x}),\,-1\Big)\,, \tag{2.27}$$

and impose the s-wave unitarity condition $|{\rm Re}a_0|<1/2$ on the maximal eigenvalue. Thus, we derive the perturbative unitarity bound on the scattering energy,

$$E \,<\, \Lambda_{\rm U1} \,=\, \frac{\sqrt{16\pi}\,v}{[\,|\widehat{x}|(1+\sqrt{1+3(1-\widehat{x})^2}\,)\,]^{1/2}}\,. \tag{2.28}$$

We plot this bound $\Lambda_{\rm U1}$ as a function of $\widehat{x}$ in Fig. 2(a), where the blue region (including the overlap with red region) denotes perturbative unitarity violation. We also show the dependence of unitarity bound on the effective cutoff $\tilde{\Lambda}_2$ of the dimension-6 operator $\mathcal{O}_{\Phi,2}$ in plots (b) and (c) for $x_2>0$

and $x_2 < 0$, respectively. For small $|\widehat{x}|$, we find $\Lambda_{\rm U1} \approx \sqrt{16\pi/3}\,\tilde{\Lambda}_2$ at leading order. As mentioned earlier, $\widehat{x}$ could be constrained by measurements of Higgs-gauge coupling in single Higgs production due to its contribution to the rescaling of Higgs kinetic term. But, given the contributions from other dimension-6 operators to the Higgs-gauge coupling and their possible large cancellations with that of $\mathcal{O}_{\Phi,2}$, the Higgs-gauge coupling could be SM-like while x_2 is more or less free from this constraint. In this case, $\mathcal{O}_{\Phi,2}$ still receives general perturbative unitarity bound from high energy scattering processes involving its induced derivative Higgs self-couplings, even though Higgs rescaling effect may be negligible. Thus, we derive the corresponding unitarity bound by turning off the Higgs rescaling effect in (2.26),

$$E \;<\; \Lambda'_{\rm U1} \;=\; \frac{\sqrt{16\pi}\,v}{3^{1/4}|\widehat{x}|^{1/2}}\,. \tag{2.29}$$

We depict the upper bound (2.29) by the blue dashed curve in Fig. 2(a)-(c). We see that $\Lambda'_{\rm U1}$ turns out to be weaker than the bound $\Lambda_{\rm U1}$. In the later analysis of dihiggs production via vector boson fusion, we will be conservative and select signal events by imposing the weaker bound $\sqrt{\hat{s}} < \Lambda'_{\rm U1}$.

Fig. 3 presents Feynman diagrams for $\bar{t}t \to hh\,(V_L V_L)$ scattering, where $V = W^\pm, Z^0$. In high energy limit, the leading amplitudes from dimension-6 operator $\mathcal{O}_{\Phi,2}$ are enhanced by E^1 terms. According to equivalence theorem, we compute the leading amplitudes with final state $V_L V_L$ replaced by the corresponding Goldstone bosons. Among all contributions, the amplitudes with t/u-channel quark-exchange and the SM Yukawa coupling approach constant in high energy limit. Only the s-channel Higgs-exchange with cubic derivative Higgs coupling in (2.10) gives the $\mathcal{O}(E^1)$ asymptotical behavior and may violate perturbative unitarity. To derive the optimal bound, we define the spin-0 and color-singlet helicity state of top-quark pair, i.e., $|\bar{t}t\rangle_s = \dfrac{1}{\sqrt{2N_c}}\displaystyle\sum_{a=1}^{N_c}\left(\left|\bar{t}^a_+ t^a_+\right\rangle - \left|\bar{t}^a_- t^a_-\right\rangle\right)$ [41]. Thus, we compute the scattering amplitudes at the leading $\mathcal{O}(E^1)$,

$$\begin{aligned}
\mathcal{T}[|\bar{t}t\rangle_s \to \left|\pi^+\pi^-\right\rangle] \;&=\; \mathcal{T}[|\bar{t}t\rangle_s \to \left|\pi^0\pi^0\right\rangle] \;=\; -\sqrt{6}\,\widehat{x}\,\zeta^2\,\frac{m_t E}{v^2}\,,\\
\mathcal{T}[|\bar{t}t\rangle_s \to |hh\rangle] \;&=\; -\sqrt{6}\,\widehat{x}\,\zeta^4\,\frac{m_t E}{v^2}, \qquad \mathcal{T}[|\bar{t}t\rangle_s \to \left|\pi^0 h\right\rangle] \;=\; \mathcal{O}(E^0)\,,
\end{aligned} \tag{2.30}$$

where E is center of mass energy. To optimize the unitarity bound, we can further define an $O(4)$ singlet final state $|S\rangle = \frac{1}{\sqrt{8}}\left(2\,|\pi^+\pi^-\rangle + \left|\pi^0\pi^0\right\rangle + |hh\rangle\right)$. So, we derive,

$$\mathcal{T}[|\bar{t}t\rangle_s \to |S\rangle] \;=\; -\widehat{x}(1-\widehat{x})(4-\widehat{x})\,\frac{\sqrt{3}m_t E}{2v^2}\,. \tag{2.31}$$

Using (2.25), we compute the partial wave amplitude and impose the s-wave unitarity condition $|\mathrm{Re}\,a_0| < \frac{1}{2}$. With these we deduce the perturbative unitarity bound on scattering energy E,

$$E \;<\; \Lambda_{\rm U2} = \frac{16\pi v^2}{\sqrt{3}m_t}\,\frac{1}{|\widehat{x}(1-\widehat{x})(4-\widehat{x})|}\,. \tag{2.32}$$

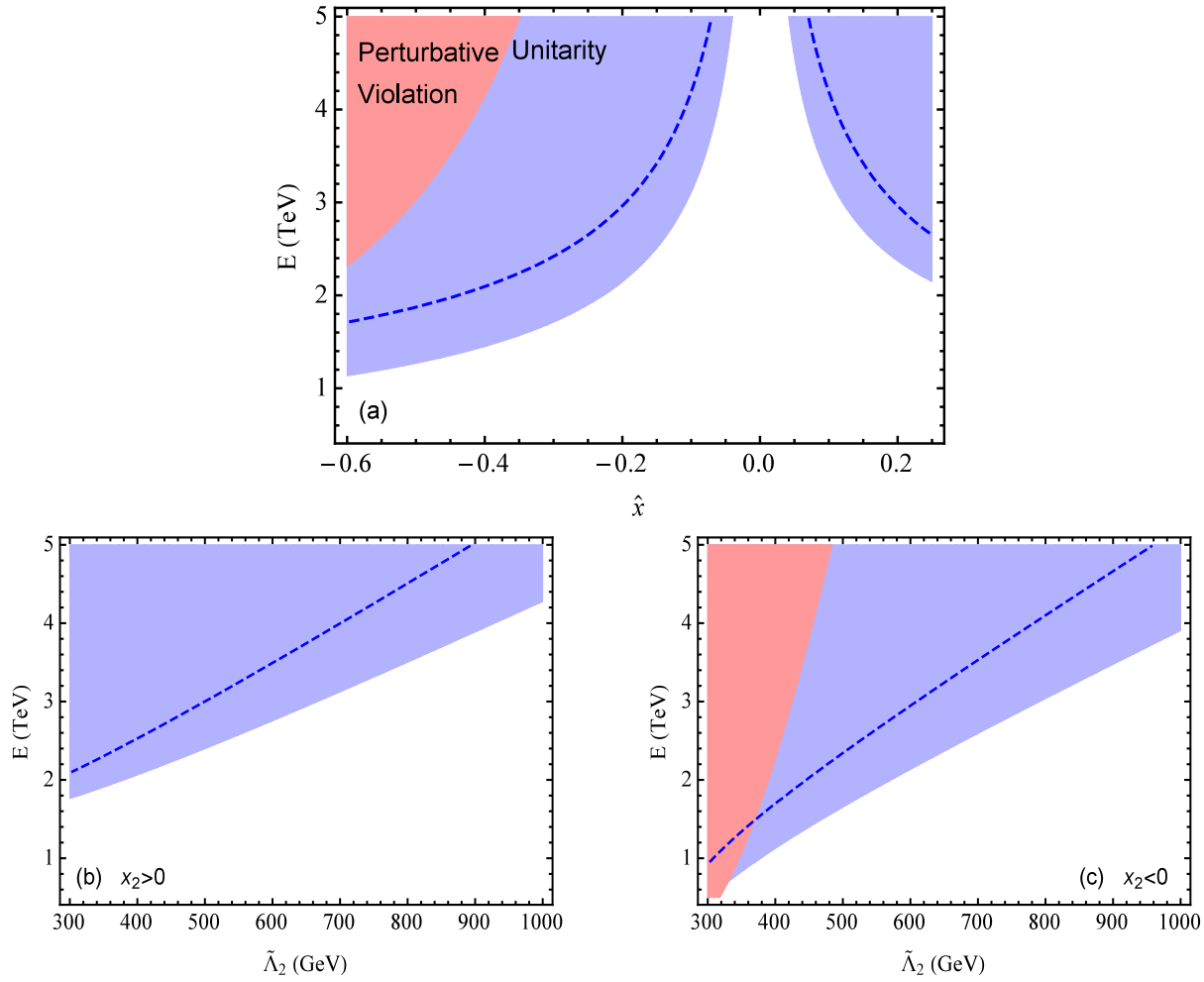

Figure 2: Perturbative unitarity violation region from weak boson scattering (blue) and top-Higgs scattering (red) as a function of $\widehat{x}$ in plot-(a), and a function of $\tilde{\Lambda}_2$ in plots (b) and (c) for $x_2 > 0$ and $x_2 < 0$, respectively.

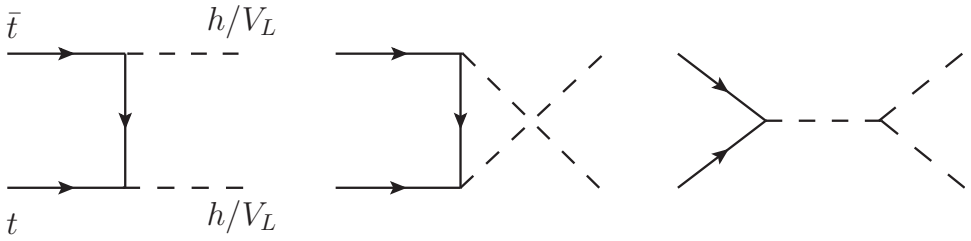

Figure 3: Feynman diagrams for $\bar{t}t \to hh\,(V_L V_L)$ scattering, where $V = W^{\pm}, Z^0$.

We plot the upper bound $\Lambda_{\rm U2}$ in Fig. 2 (red contours) as a function of $\widehat{x}$ and $\tilde{\Lambda}_2$, respectively. For small $|\widehat{x}|$, we derive $\Lambda_{\rm U2} \approx 4\pi\tilde{\Lambda}_2^2/\sqrt{3}m_t$ at leading order. It is clear that the bound from top-Higgs scattering is much weaker than that of the weak boson scattering.

3. Higgs Pair Production at Hadron Colliders

In this section, we study dihiggs production for the effective theory defined in Eq. (2.16) at both the LHC (14 TeV) and future pp (100TeV) collider. There are two new parameters (x_2, x_3), which may be reparametrized as ($\widehat{x}$, $\widehat{r}$) in Eq. (2.11) for convenience. The major dihiggs production channels at high energy hadron collider include gluon fusion production ($gg \to hh$), top-pair associated production ($pp \to t\bar{t}hh$), and VBF production ($pp \to hhjj$). In the following, we analyze these production channels at parton level, and compare their differences in total cross sections and in kinematical distributions over the parameter space of ($\widehat{x}$, $\widehat{r}$).

With the modified cubic Higgs couplings (2.10) from dimension-6 operators, we derive the differential cross section for gluon fusion production,

$$\frac{d\hat{\sigma}(gg \to hh)}{d\hat{t}} = \frac{G_F^2 \alpha_s^2}{512(2\pi)^3}\, \zeta^4 \left[\left| \left((1+\widehat{r}\,) \frac{3m_h^2}{\hat{s}-m_h^2} - \widehat{x}\, \frac{\hat{s}+2m_h^2}{\hat{s}-m_h^2} \right) F_\triangle + F_\square \right|^2 + |G_\square|^2 \right], \tag{3.33}$$

where ($\hat{s}$, $\hat{t}$) are partonic Mandelstam variables, and ($F_\triangle$, $F_\square$, $G_\square$) are loop functions given in Appendix B, The new contributions from x_2 ($\widehat{x}$) arise in two ways. The first is an overall rescaling factor ζ^4 of the cross section, and the second is contributed by the derivative cubic Higgs coupling. The parameter x_3 only appears in $\widehat{r}$, which shifts the SM cubic Higgs coupling. We generate signal events by MadGraph 5 [42].[7] The QCD corrections can be significant [43], but they are insensitive to the structure of cubic Higgs coupling,[8] so we normalize the cross section at $(\widehat{r}, \widehat{x}) = (0, 0)$ to the SM NLO prediction [17] and implement the same K-factor for full parameter space of $(\widehat{r}, \widehat{x})$. For gluon fusion, we have $K = (2.27, 1.44)$ for $\sqrt{s} = (14, 100)$ TeV. But, for analyzing the *ratio* of the cross section over that of the SM, it is rather insensitive to the K-factor. We perform numerical fits for the total cross sections over the range $-1 \leqslant \widehat{r} \leqslant 1$ and $-1 \leqslant \widehat{x} \leqslant 0.5$ at both LHC (14TeV) and pp (100TeV) collider,

$$\left.\frac{\sigma(gg \to hh)}{\sigma(gg \to hh)_{\rm sm}}\right|_{\rm 14TeV} = (1-\widehat{x})^2 \left(1 - 0.83\,\widehat{r} + 3.7\,\widehat{x} + 0.29\,\widehat{r}^2 + 4.2\,\widehat{x}^2 - 2.0\,\widehat{r}\,\widehat{x}\right), \tag{3.34a}$$

$$\left.\frac{\sigma(gg \to hh)}{\sigma(gg \to hh)_{\rm sm}}\right|_{\rm 100TeV} = (1-\widehat{x})^2 \left(1 - 0.72\,\widehat{r} + 3.6\,\widehat{x} + 0.22\,\widehat{r}^2 + 4.3\,\widehat{x}^2 - 1.7\,\widehat{r}\,\widehat{x}\right). \tag{3.34b}$$

This shows that the fitted cross section ratio is not sensitive to the variation of collision energy from $\sqrt{s} = 14\,\text{TeV}$ to $\sqrt{s} = 100\,\text{TeV}$. This is mainly due to the $m_f^2/\hat{s}$ suppression in the loop functions $F_\triangle$ and $F_\square$ under high energy limit [cf. Eq. (B.52)]. Expanding (3.33) around the SM values $(\widehat{r}, \widehat{x}) = (0, 0)$, we derive the $\widehat{r}$ dependence, $d(\sigma/\sigma_{\rm sm})/d\widehat{r} \simeq -(0.7-0.8)$. For the parameter

[7] To include the effect of finite top mass, we use the model file SMEFT_FF_bt for events generation. The relevant code is available at https://cp3.irmp.ucl.ac.be/projects/madgraph/wiki/HiggsPairProduction.

[8] As shown in Ref.[44], for various dimension-6 operators relevant for gluon fusion production, the correction to the K-factor is around several per cent.

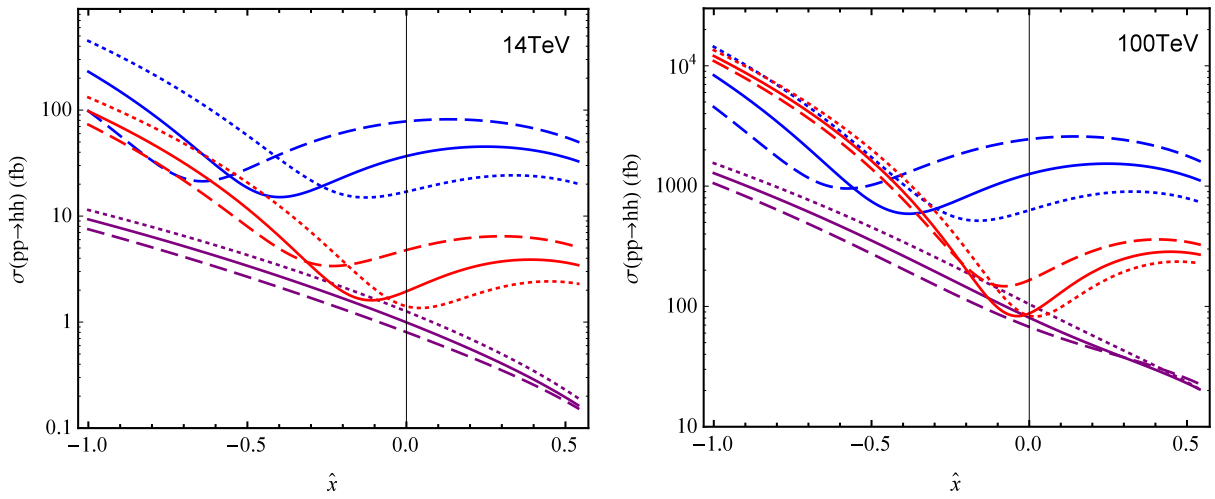

Figure 4: Cross sections of dihiggs production via gluon fusion (blue), top-pair associated production (purple) and vector boson fusion (red) at the LHC (14TeV) (left plot) and pp(100TeV) collider (right plot). For each production channel, the (dashed, solid, dotted) curves depict cross sections as functions of $\widehat{x}$ under three inputs of $\widehat{r} = (-1,\, 0,\, 1)$.

$\widehat{x}$, the prefactor $(1-\widehat{x})^2 = \zeta^4$ in Eq. (3.34) comes from rescaling factors of Higgs fields hh in the final state, while $\widehat{x}$ in the second parentheses is contributed by the derivative cubic Higgs coupling. We note that these two contributions have some cancellation. For $\widehat{x} > 0$ ($\widehat{x} < 0$), the contribution from derivative coupling interferes constructively (destructively) with the SM part of $(\widehat{r},\, \widehat{x}) = (0,\, 0)$, while the total cross section is suppressed (enhanced) by the Higgs rescaling factor $(1-\widehat{x})^2$. The blue curves in Fig. 4 depict the gluon fusion cross sections at pp(14TeV) and pp(100TeV). The (dashed, solid, dotted) curves present the cross sections varying with $\widehat{x}$, under inputs $\widehat{r} = (-1,\, 0,\, 1)$, respectively. From Fig. 4, we see that the dihiggs production cross sections from gluon fusion exhibit a minimum in the $\widehat{x} < 0$ region, and the location of this minimum varies with the input value of $\widehat{r}$.

In Fig. 5, using MadAnalysis-5 package [45], we present the normalized kinematic distribution of final state Higgs bosons at pp(100 TeV) collider. The first column display the leading Higgs $p_T(h)$ distributions; while the second column depict the M_{hh} invariant-mass distributions of the Higgs pair. The shapes of distributions at the LHC(14TeV) and pp (100TeV) collider have some similarity since the cross section only has mild energy dependence. In the first row of Fig. 5, we have input $\widehat{r} = 0$, and the (blue, red, green) curves correspond to $\widehat{x} = (-1,\, 0,\, 0.5)$; while the second row has $\widehat{x} = -1$, and (blue, red, green) curves correspond to $\widehat{r} = (-1,\, 0,\, 1)$. For the parameter range $\widehat{x} < 0$, there is large cancellation between the SM box-loop diagram and the triangle-loop diagram with s-channel Higgs and new derivative cubic Higgs coupling over the intermediate momentum range. This makes the distribution more sensitive to $\widehat{r}$. In particular, if we turn off the SM cubic Higgs coupling by

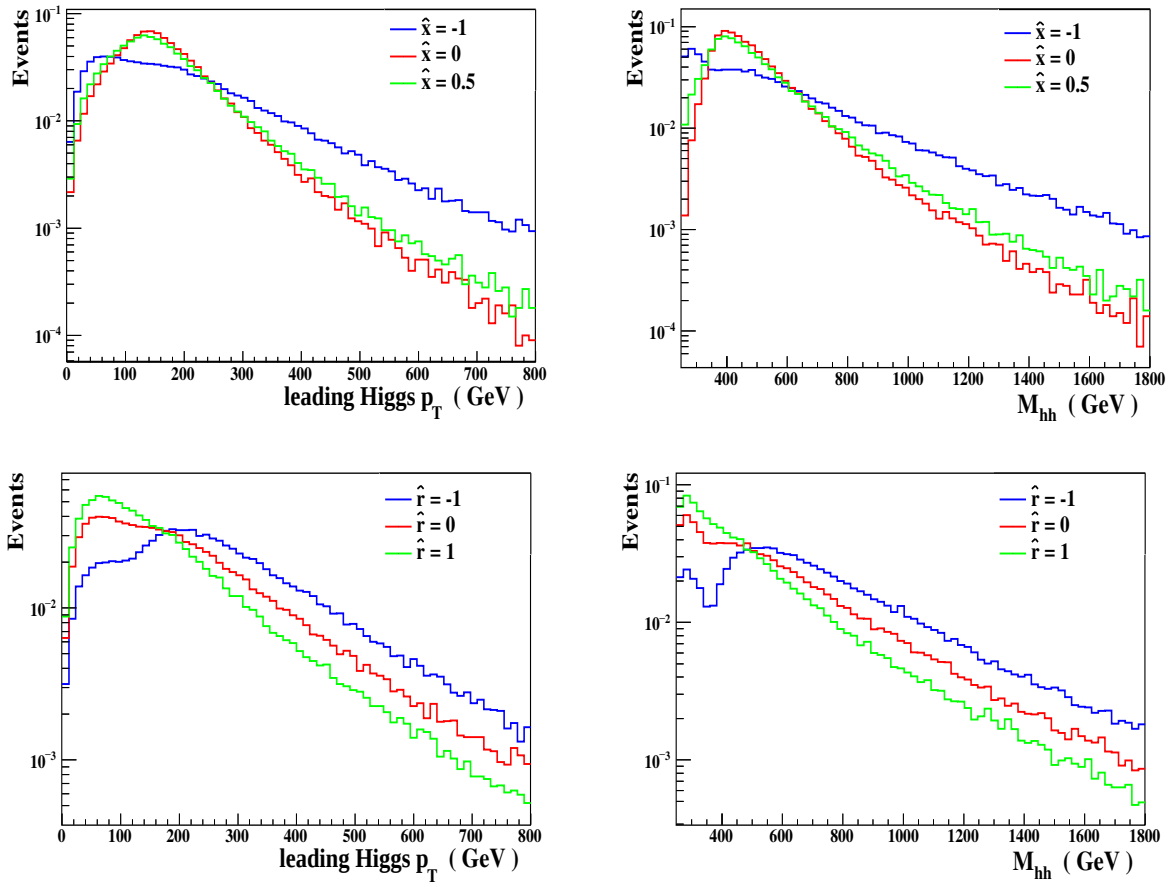

Figure 5: Parton level distributions of $gg \to hh$ for the leading Higgs p_T (1st column) and the invariant-mass M_{hh} (2nd column) at pp(100TeV). In the first row, we input $\widehat{r} = 0$, and the (blue, red, green) curves correspond to $\widehat{x} = (-1,\, 0,\, 0.5)$. In the second row, we input $\widehat{x} = -1$, and the (blue, red, green) curves correspond to $\widehat{r} = (-1,\, 0,\, 1)$.

setting $\widehat{r} = -1$, the events are mostly populated in large p_T and M_{hh} regions, as shown by the blue curves in the second row of Fig. 5. For $\widehat{x} > 0$ and $\widehat{r} > -1$, all contributions add to each other constructively, and the normalized distributions do not significantly change.[9]

Next, we consider the top-pair associated dihiggs production. The dependence of its cross section on $(x_2,\, x_3)$ can be reparametrized in terms of $(\widehat{x},\, \widehat{r})$, and is similar to that of (3.33). We generate the signal events by MadGraph 5, and find the factor $K = 1.2$ for total cross sections at both the LHC (14TeV) and pp (100TeV) collider [17]. We perform numerical fits of total cross sections for

[9] In passing, Ref.[46] studied interference between the SM cubic Higgs coupling and other SM contributions in a few dihiggs production channels, with focus on the variations of collision energy and parton distribution function.

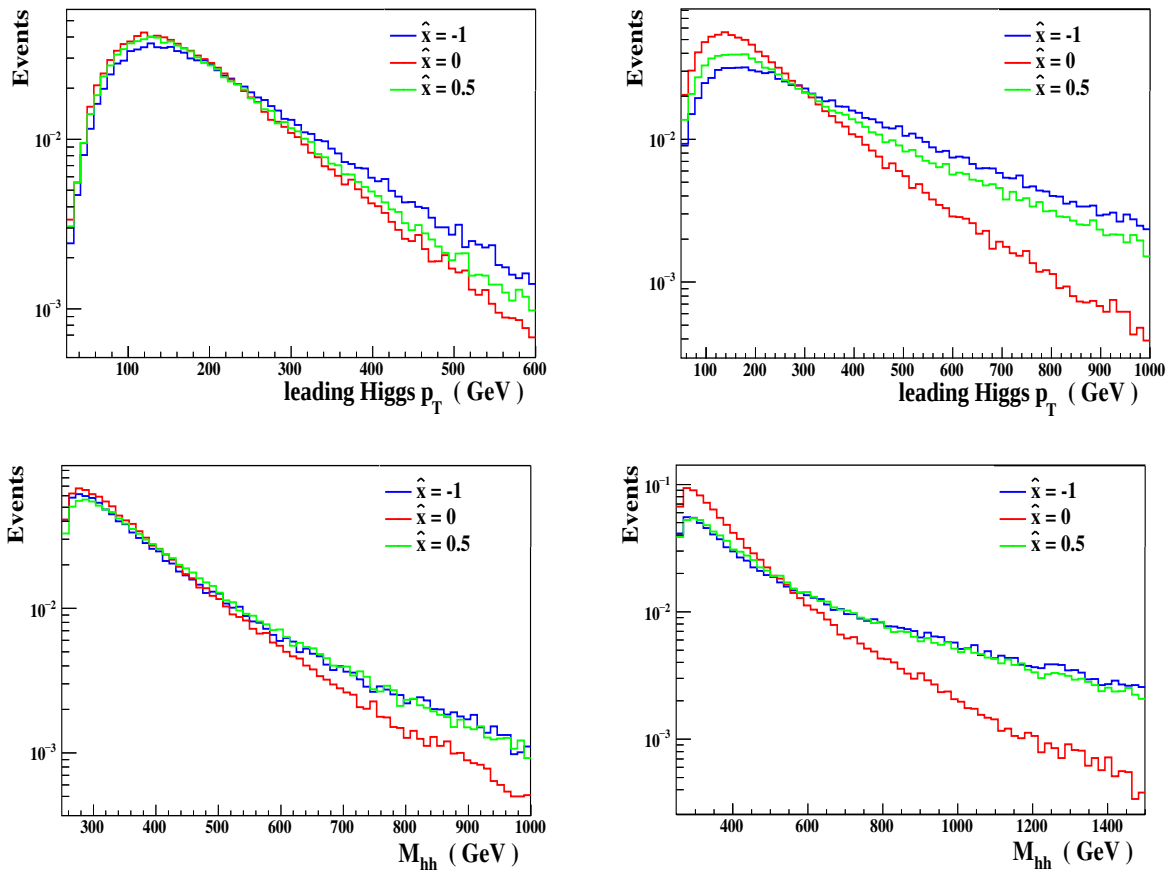

Figure 6: Parton level distribution of $pp \to t\bar{t}hh$ for the leading p_T distributions of Higgs boson (1st row), the invariant-mass distributions M_{hh} (2nd row) at the LHC(14TeV) (1st column) and the pp(100TeV) (2nd column). In each plot, we set $\widehat{r} = 0$, and input $\widehat{x} = (-1,\, 0,\, 0.5)$ which correspond to (blue, red, green) curves, respectively.

$-1 \leqslant \widehat{r} \leqslant 1$ and $-1 \leqslant \widehat{x} \leqslant 0.5$, which are summarized as follows,

$$\left.\frac{\sigma(pp \to \bar{t}thh)}{\sigma(pp \to \bar{t}thh)_{\rm sm}}\right|_{14\rm TeV} = (1-\widehat{x})^2\big(1 + 0.23\,\widehat{r} - 0.73\,\widehat{x} + 0.04\,\widehat{r}^2 + 0.60\,\widehat{x}^2 - 0.26\,\widehat{r}\,\widehat{x}\big), \tag{3.35a}$$

$$\left.\frac{\sigma(pp \to \bar{t}thh)}{\sigma(pp \to \bar{t}thh)_{\rm sm}}\right|_{100\rm TeV} = (1-\widehat{x})^2\big(1 + 0.23\,\widehat{r} - 0.80\,\widehat{x} + 0.07\,\widehat{r}^2 + 2.2\,\widehat{x}^2 - 0.54\,\widehat{r}\,\widehat{x}\big). \tag{3.35b}$$

In comparison with the dihiggs production via gluon fusion, the cross section of top-pair associated production is less sensitive to the change of either $\widehat{r}$ or $\widehat{x}$, due to the dominance of diagrams irrelevant to Higgs self-interaction. But, the $\widehat{x}$-dependence of top-pair associated production cross section is much more sensitive to the increase of collision energy than that of gluon fusion production, especially for the $\widehat{x}^2$ term. We note that the derivative cubic Higgs coupling term interferes destructively (constructively) with the SM t/u-channel exchange of top for $\widehat{x} > 0$ ($\widehat{x} < 0$). Hence, this process

is complementary to gluon fusion production. In Fig. 4, we plot the total cross sections of top-pair associated dihiggs production by purple curves. It is much suppressed in $\widehat{x} > 0$ region due to the overall rescaling factor $(1-\widehat{x})^2 = \zeta^4$. For $\widehat{r} > 0$, it adds positive contributions to that of the SM, and makes the test of $\widehat{r}$ easier [23].

We present in Fig. 6 the normalized kinematic distributions for top-pair associated dihiggs production at parton level. The first row shows the leading p_T distribution of the Higgs boson, and the second row depicts the dihiggs invariant-mass (M_{hh}) distribution, at the LHC (14TeV) (in first column) and pp(100TeV) collider (in second column). At the LHC, they are rather insensitive to the variation of $(\widehat{x}, \widehat{r})$. However, the pp (100TeV) collisions significantly improve the sensitivity to $\widehat{x}$. In comparison with the dihiggs production via gluon fusion in Fig. 5, the top-pair associated production is more sensitive to the derivative cubic Higgs coupling, with more signal events populated in the higher p_T and larger M_{hh} region. To maintain perturbative unitarity, we will require signal events to obey $M_{hh} < \Lambda_{\rm U2}$, where $\Lambda_{\rm U2}$ is derived in (2.32). We find that this bound at $\widehat{x} = 0.5$ is too weak to be relevant; and there are 77% (97%) signal events passed this requirement for $\widehat{x} = -1$ at $\sqrt{s} = 100\,\text{TeV}$ (14 TeV).

Finally, we turn to the dihiggs production via vector boson fusion, $pp \to V^*V^*jj \to hhjj$. Its cross section depends on (x_2, x_3) through the overall rescaling factor ζ^4, the modified (SM-like) cubic Higgs coupling $\widehat{r}$, and the new derivative cubic Higgs couplings $\widehat{x}$. We generate signal events by Madgraph 5 with electroweak process, and apply the following VBF cuts to two tagging jets [47],

$$14\,\text{TeV}: \quad 2 < |\eta_j| < 5\,, \quad \eta_{j_1}\cdot\eta_{j_2} < 0\,, \quad p_{T,j} > 25\,\text{GeV}, \quad M_{jj} > 500\,\text{GeV}; \tag{3.36a}$$

$$100\,\text{TeV}: \quad 2 < |\eta_j| < 5\,, \quad \eta_{j_1}\cdot\eta_{j_2} < 0\,, \quad p_{T,j} > 50\,\text{GeV}, \quad M_{jj} > 1000\,\text{GeV}. \tag{3.36b}$$

We perform numerical fits to the total cross section for $-1 \leqslant \widehat{r} \leqslant 1$ and $-1 \leqslant \widehat{x} \leqslant 0.5$, and derive the following,[10]

$$\left.\frac{\sigma(pp\to hhjj)}{\sigma(pp\to hhjj)_{\rm sm}}\right|_{14\rm TeV} = (1-\widehat{x})^2\big(1 - 0.86\,\widehat{r} + 4.8\,\widehat{x} + 0.59\,\widehat{r}^2 + 16\,\widehat{x}^2 - 4.6\,\widehat{r}\,\widehat{x}\big), \tag{3.37a}$$

$$\left.\frac{\sigma(pp\to hhjj)}{\sigma(pp\to hhjj)_{\rm sm}}\right|_{100\rm TeV} = (1-\widehat{x})^2\big(1 - 0.47\,\widehat{r} + 4.6\,\widehat{x} + 0.42\,\widehat{r}^2 + 38\,\widehat{x}^2 - 4.1\,\widehat{r}\,\widehat{x}\big). \tag{3.37b}$$

We find that the cross section of VBF channel is much more sensitive to $\widehat{x}$ than the other two processes discussed above. After implementing VBF cuts, the cross section is dominated by longitudinal weak boson scattering, and the amplitude has E^2 enhancement which greatly improves the signal sensitivity to $\widehat{x}$ in pp(100TeV) collisions. In Fig. 4, we present the cross sections by red curves at

[10] For the *ratio* between the VBF signal cross sections in Eq. (3.37), we note that the QCD K-factors are largely cancelled out and thus this ratio is very insensitive to the K-factors.

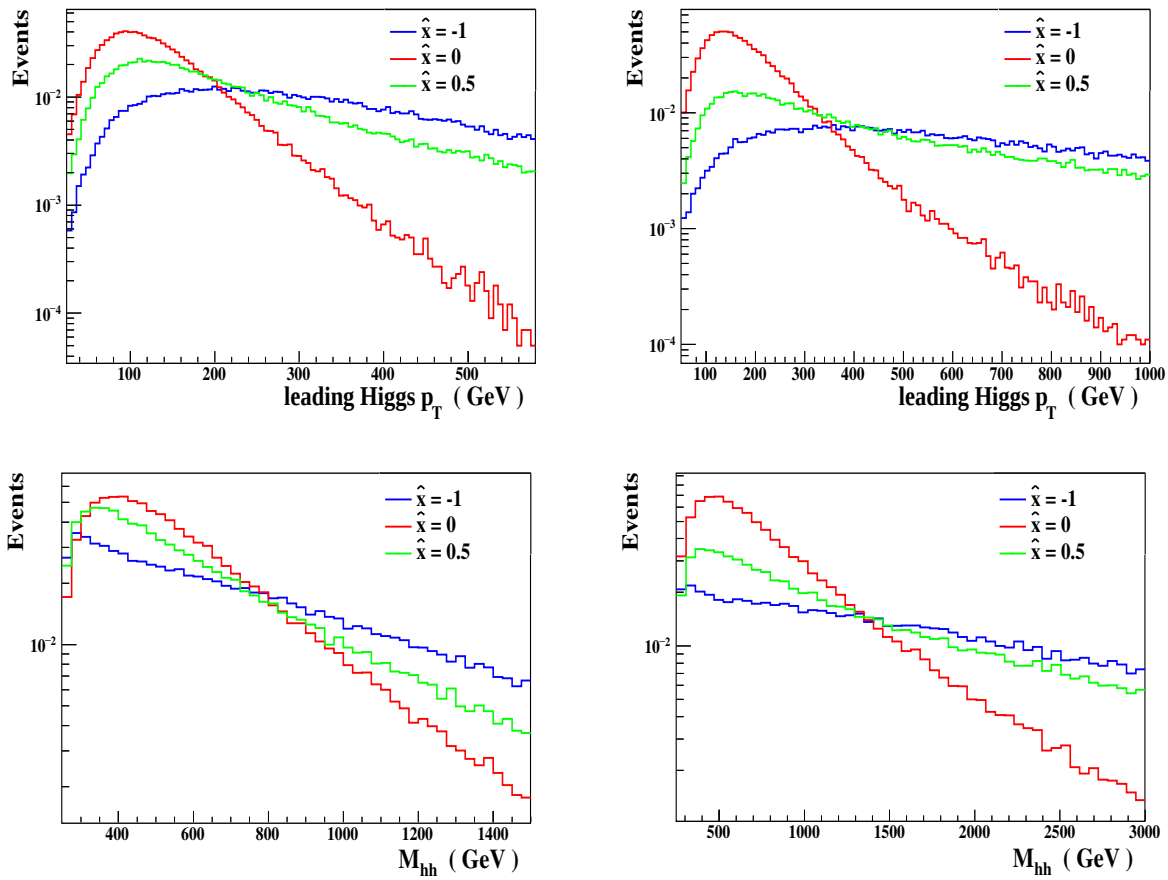

Figure 7: Parton level distributions of $pp \to V^*V^*jj \to hhjj$ for the leading p_T of Higgs boson (first row), the invariant-mass M_{hh} (second row) at LHC (14TeV) (first column), and pp(100TeV) (second column). In each plot, we set $\widehat{r} = 0$, and input $\widehat{x} = (-1,\, 0,\, 0.5)$ which correspond to (blue, red, green) curves.

the LHC (14TeV) and pp(100TeV) collider. These cross sections are normalized to the NLO SM prediction [17] at $(\widehat{r},\, \widehat{x}) = (0,\, 0)$. The total cross sections become comparable to that of the gluon fusion production over large negative $\widehat{x}$ region, but their dependence on $\widehat{r}$ is weaker.

In Fig. 7, we present the distributions for the leading p_T of Higgs boson (first row), the dihiggs invariant-mass M_{hh} (second row) at the LHC (14TeV) (first column) and pp (100TeV) collider (second column). In comparison with top-pair associated production of Fig. 6, more signal events are populated in the high p_T and M_{hh} regions for $\widehat{x} \neq 0$, which is notable even at the LHC (14TeV). To further ensure the perturbative expansion of the present effective theory, we will take into account the unitarity constraint. We require signal events to obey the conservative bound $M_{hh} > \Lambda'_{\rm U1}$ in (2.29). For $\sqrt{s} = 14$TeV (100TeV) collisions, this allows 84% (31%) signal events under $\widehat{x} = -1$, and 97% (62%) signal events under $\widehat{x} = 0.5$.

4. Full Analysis of $gg \to hh \to b\bar{b}\gamma\gamma$ at pp(100TeV) Collider

In this section, we study dihiggs production via gluon fusion by performing a full analysis (including Delphes 3 fast detector simulations) at the pp (100TeV) collider. We will focus on the channel $gg \to hh \to b\bar{b}\gamma\gamma$. Our analysis extends the previous Snowmass study [6] by including non-SM-like derivative cubic Higgs coupling via model-independent dimension-6 effective operators. We also present a full background study which further includes jet-faking-photon backgrounds and contributions of $jj\gamma\gamma$ due to mis-tagging b or $\bar{b}$. These improve the analysis of Ref. [6].

4.1. Full Simulations for Signals and Backgrounds

For the present study, we generate the signal and background events by using Madgraph 5 and Pythia 6.2 packages [42][48], which are then passed to Delphes 3 for detector simulations [49].

We show the full list of backgrounds in Table 1. All background processes include up to one extra parton with MLM matching to avoid double-counting. We do not include $b\bar{b}jj$ background, since after all selection cuts it is negligible compared with other faked backgrounds. The detector responses are based on the current performance of ATLAS and CMS. The b-tagging operation point is chosen to have 75%, 18.8%, and 1% for bottom, charm, and light flavor jets in the central region ($E_T > 50\,\text{GeV}$ and $|\eta| < 2.5$), respectively. The photon identification efficiency is about 80% for photons with $E_T > 50\,\text{GeV}$ and $|\eta| < 2.5$. For the jet-faking-photon background, we assign a faking probability of $f_j = 0.0093\exp(-E_T/27)$ as a function of E_T (in GeV) of the jet, and scale the jet energy by 0.75 ± 0.12 as the photon energy [50]. The mass resolution is 2 GeV for $h \to \gamma\gamma$ and 17 GeV for $h \to b\bar{b}$ at $M_h = 125\,\text{GeV}$. To be consistent with the signal, we select two tagged b-jets and two isolated photons in the final states, where each object is required to have $E_T > 25\,\text{GeV}$ and $|\eta| < 2.5$.

We further impose the mass-window cuts on the invariant-masses of two photons and two b-jets. Compared with the previous study [6], we will narrow down the diphoton invariant-mass window as $122\,\text{GeV} < M_{\gamma\gamma} < 128\,\text{GeV}$. This would kill another 40% backgrounds beyond the previous case with 10 GeV diphoton mass-window. For two b-jets, we still impose $85\,\text{GeV} < M_{b\bar{b}} < 135\,\text{GeV}$.

Fig. 8 shows the normalized distributions of the p_T and the sub-leading E_T of two selected photons (or b-jets) in the first two rows. The last plot of Fig. 8 depicts the reconstructed dihiggs invariant-mass $M_{b\bar{b}\gamma\gamma}$ for both signals and backgrounds. Here we only show the representative backgrounds. The distributions of faked $b\bar{b}j\gamma$ and $jj\gamma\gamma$ are similar to $b\bar{b}\gamma\gamma$, while $t\bar{t}\gamma\gamma$ and $t\bar{t}\gamma$ have too few events after selection. For illustration, we present distributions for the SM and two other cases with new coupling inputs $(\widehat{r}, \widehat{x}) = (-1, 0.5)$ and $(\widehat{r}, \widehat{x}) = (1, -1)$. We find that including the new

Table 1: For signal and background processes, this table presents $\sigma \times \mathrm{Br}$, generated events, selected events, acceptance, and the expected events at $pp\,(100\,\mathrm{TeV})$ collider with an integrated luminosity of $3\,\mathrm{ab}^{-1}$.

Samples	$\sigma \times$BR (fb)	Generated Evt	Selected Evt	Accept	Expected
$h(b\bar{b})h(\gamma\gamma)$ (SM)	3.53	100000	3955	0.040	418.8 ± 6.6
$b\bar{b}h(\gamma\gamma)$	50.49	99611	78	0.00078	118.6 ± 13.4
$Z(b\bar{b})h(\gamma\gamma)$	0.8756	68585	378	0.0055	14.5 ± 0.7
$t\bar{t}h(\gamma\gamma)$	37.26	63904	67	0.0010	117.2 ± 14.3
$t\bar{t}\gamma\gamma$	335.8	150654	1	6.6×10^{-6}	6.75 ± 6.7
$t\bar{t}\gamma$	108400	285787	0.013	4.7×10^{-8}	15.2 ± 3.2
$b\bar{b}\gamma\gamma$	5037	763962	11	1.4×10^{-5}	217.6 ± 65.6
$b\bar{b}j\gamma$	8960000	1119406	0.0051	4.6×10^{-9}	123.6 ± 31.9
$jj\gamma\gamma$	164200	813797	0.056	6.9×10^{-8}	33.9 ± 3.8
Total background	–	–	–	–	647.3 ± 76.0
$S/\sqrt{B}$ $(S/\sqrt{B+S})$	–	–	–	–	16.5 (12.8)

couplings $(\widehat{r}, \widehat{x})$ does not significantly change kinematic distributions after full simulation for the gluon fusion production, as we have expected from the parton level analysis in Sec. 3. Hence, for the rest of selections, we use the same kinematical cuts as in the Snowmass study [6].

We summarize these cuts as follows,

- Invariant-mass cut: $M_{b\bar{b}\gamma\gamma} > 300\,\mathrm{GeV}$;
- ΔR cuts: $\Delta R_{\gamma\gamma} < 2.5\,, \quad \Delta R_{b\bar{b}} < 2.0\,;$
- p_T cuts: $p_T[\gamma],\, p_T[b] > 35\,\mathrm{GeV}, \quad p_T[\gamma\gamma],\, p_T[b\bar{b}] > 100\,\mathrm{GeV}\,;$
- Decay angle of $h \to \gamma\gamma$ in the hh rest frame: $|\cos\theta_h| < 0.8\,;$[11]
- Total number n of jets, photons and leptons are required to be $n < 7$ in each event.

We present the expected signal and background event numbers at $\sqrt{s} = 100\,\mathrm{TeV}$ and for an integrated luminosity $\mathcal{L} = 3\,\mathrm{ab}^{-1}$ in Table 1. For the SM Higgs self-coupling of $(\widehat{r}, \widehat{x}) = (0, 0)$, we find the expected signal events to be 418.8. The expected yield of total background events is 647.3, with the largest contributions coming from $b\bar{b}\gamma\gamma$, $b\bar{b}j\gamma$, $b\bar{b}h(\gamma\gamma)$ and $t\bar{t}h(\gamma\gamma)$. The resultant signal statistic significance is about $16.5\,\sigma$. With some relaxation of kinematical cuts, we find that the sensitivity becomes a bit worse due to increased background contributions, but the overall picture remains the same. We have also compared our study with the recent analyses of $b\bar{b}\gamma\gamma$ channel at

[11] The decay angle θ_h is defined as the angle between one of the h directions in the dihiggs rest frame and the dihiggs momentum in the lab frame.

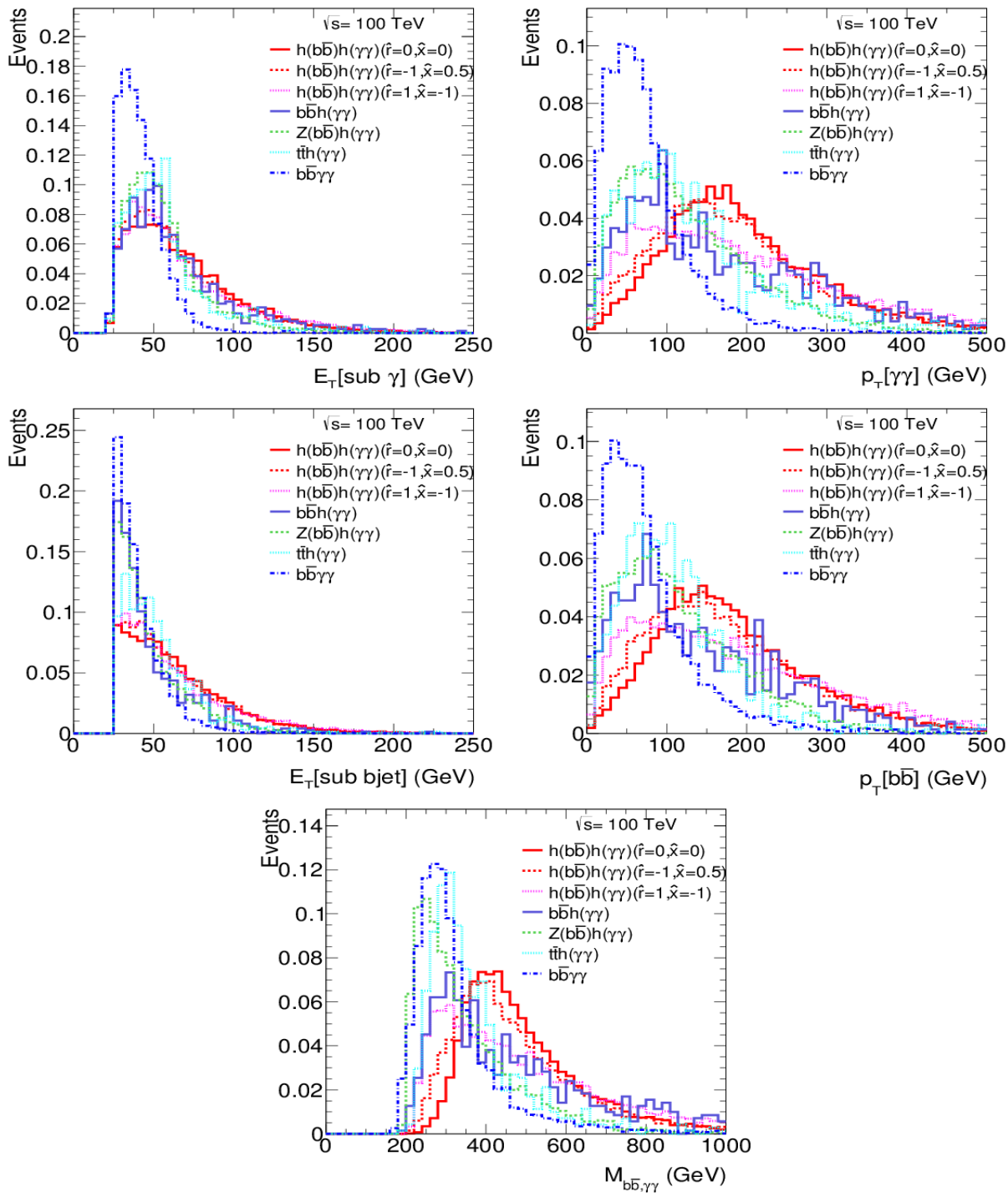

Figure 8: Distributions of the sub-leading $E_T[\text{sub}\,\gamma]$ and $p_T[\gamma\gamma]$ of selected diphotons for the signal/background events are presented in the first row. The distributions of $E_T[\text{sub}\,b\text{-jet}]$ and $p_T[b\bar{b}]$ of the selected $b\bar{b}$ jets are depicted in the second row. The invariant-mass distributions of the selected $\gamma\gamma b\bar{b}$ events are plotted in the third row.

$pp(100)$ TeV in the literature [51][25]. Ref. [51] studied this channel for the SM cubic Higgs coupling, and estimated 179 signal events with 447 background events after all cuts and for the same luminosity. Our study gives 418.8 signal events and 647.3 background events. The difference is likely due to their more conservative assumptions for the detector performance, especially the photon identification efficiency, which is lower than ours. In the future, it would be helpful to directly compare the results by using the same assumptions for detector performance. Ref. [25] estimated $S/\sqrt{B} = 15.2$ under all cuts and the same condition, which is in good agreement with ours.

For the signal analysis, we perform full simulations for parameters within the range $-1 \leqslant \widehat{r} \leqslant 1$ and $-1 \leqslant \widehat{x} \leqslant 0.5$. We find that the number of selected signal events can be fitted by similar functions as in Eq. (3.34). Under the above cuts, we deduce

$$\left.\frac{\sigma}{\sigma_{\rm sm}}\right|_{\rm All} = (1-\widehat{x})^2\big(1 - 0.55\,\widehat{r} + 3.4\,\widehat{x} + 0.11\,\widehat{r}^2 + 3.9\,\widehat{x}^2 - 1.2\,\widehat{r}\,\widehat{x}\big)\,. \tag{4.38}$$

Compared with the parton level fit (3.34b), we see that the cross section becomes less sensitive to the parameters $(\widehat{r}, \widehat{x})$. This is what we would expect from the contamination of parton shower, hadronization, and detector simulation.

To further discriminate $\widehat{r}$ and $\widehat{x}$ dependence, we can utilize distributions in different reconstructed dihiggs invariant-mass bins [27, 25], which include different kinematic features of contributions from $\widehat{r}$ and $\widehat{x}$. To efficiently suppress the background, we choose $M_{hh}(= M_{b\bar{b}\gamma\gamma})$ bins as follows,

$$M_{hh} \text{ bins (GeV):} \quad [300, 500],\ [500, 700],\ [700, 900],\ [900, 1100]. \tag{4.39}$$

We note that for the $b\bar{b}\gamma\gamma$ final state, due to the small branching fraction of $h \to \gamma\gamma$ and the fast decline of gluon parton distribution function, the probe of M_{hh} is not much higher than 1 TeV even at the $pp\,(100\text{TeV})$ collider. Since the derivative cubic Higgs coupling brings in more energy enhancement, higher M_{hh} bin is more sensitive to $\widehat{x}$. This can be seen from event fits in each bin as follows,

$$\left.\frac{\sigma}{\sigma_{\rm sm}}\right|_{\rm bin\,1} = (1-\widehat{x})^2(1 - 0.82\,\widehat{r} + 3.4\,\widehat{x} + 0.17\,\widehat{r}^2 + 3.3\,\widehat{x}^2 - 1.5\,\widehat{r}\,\widehat{x})\,, \tag{4.40a}$$

$$\left.\frac{\sigma}{\sigma_{\rm sm}}\right|_{\rm bin\,2} = (1-\widehat{x})^2(1 - 0.42\,\widehat{r} + 3.3\,\widehat{x} + 0.06\,\widehat{r}^2 + 3.8\,\widehat{x}^2 - 0.95\,\widehat{r}\,\widehat{x})\,, \tag{4.40b}$$

$$\left.\frac{\sigma}{\sigma_{\rm sm}}\right|_{\rm bin\,3} = (1-\widehat{x})^2(1 - 0.14\,\widehat{r} + 3.5\,\widehat{x} + 0.04\,\widehat{r}^2 + 5.6\,\widehat{x}^2 - 0.85\widehat{r}\,\widehat{x})\,, \tag{4.40c}$$

$$\left.\frac{\sigma}{\sigma_{\rm sm}}\right|_{\rm bin\,4} = (1-\widehat{x})^2(1 - 0.03\,\widehat{r} + 4.0\,\widehat{x} + 0.03\,\widehat{r}^2 + 8.6\,\widehat{x}^2 - 0.65\,\widehat{r}\,\widehat{x})\,. \tag{4.40d}$$

With increasing M_{hh}, the coefficients of $\widehat{r}$ terms decrease, while $\widehat{x}$ terms become more important. In passing, we clarify the difference of our analysis from Ref. [25]. The paper [25] simplifies the

computation by doing hadron-level analysis for the SM case only, and infers the signal rate at other points by parton-level analysis with rescaling of hadron-to-parton ratio for the SM, i.e., they assumed that the hadron-to-parton cuts efficiency remains the same over the parameter space. We test this assumption with our full analysis in the $\widehat{r}-\widehat{x}$ parameter space. We find that it works well in lower M_{hh} bins, but would induce $\mathcal{O}(10\%-100\%)$ deviations in high mass bins [12]. For the inclusive rate, it is not a problem since it is dominated by low mass bins. But, it could affect the conclusion of exclusive analysis (cf. Sec. 4.2). For later convenience, we summarize the numbers of selected background events for each bin in Table 2.

4.2. Probing Cubic Higgs Interactions via Parameter Space $(\widehat{r},\,\widehat{x})$

In this section, we analyze the probe of $\widehat{r}-\widehat{x}$ parameter space at the $pp\,(100\,\text{TeV})$ collider with a sample data from $3\,\text{ab}^{-1}$ $(30\,\text{ab}^{-1})$ integrated luminosity. As mentioned in Sec. 2, due to interferences with other possible dimension-6 operators, the measurement of single Higgs productions cannot uniquely constrain $\widehat{x}$. Hence, it is important to independently probe the parameter space of $\widehat{x}$ via dihiggs production, which receives energy enhancement from the derivative coupling induced by $\mathcal{O}_{\Phi,2}$. To study sensitivities to different regions of the $(\widehat{r},\,\widehat{x})$ parameter space, we choose four kinds of benchmark points,

$$\begin{aligned}
\text{Benchmark A}: &\quad (\widehat{r},\,\widehat{x})_{\text{sm}} = (0,\,0)\,;\\
\text{Benchmarks B}_1,\,\text{B}_2: &\quad (\widehat{r},\,\widehat{x}) = (0,\,0.2),\,(0,\,0.5)\,;\\
\text{Benchmarks C}_1,\,\text{C}_2: &\quad (\widehat{r},\,\widehat{x}) = (-0.5,\,0),\,(0.5,\,0)\,;\\
\text{Benchmarks D}_1,\,\text{D}_2: &\quad (\widehat{r},\,\widehat{x}) = (-0.5,\,0.2),\,(0.5,\,-0.5)\,.
\end{aligned} \tag{4.41}$$

Benchmark A corresponds to the SM Higgs boson, and the sensitivity in this case can be directly translated into a bound on the effective cutoffs of dimension-6 operators $(\mathcal{O}_{\Phi,2},\,\mathcal{O}_{\Phi,3})$. We use Benchmarks B_1 and B_2 to represent the cases as predicted by nonminimal coupling model with $\widehat{r}=0$ and $\widehat{x}>0$ (cf. Sec. 2.2). Benchmarks C_1 and C_2 correspond to nonzero $\widehat{r}$ and vanishing derivative cubic Higgs coupling $\widehat{x}$. The last two benchmarks D_1 and D_2 denote the general cases with both $\widehat{r}$ and $\widehat{x}$ nonzero. For all non-SM benchmarks, we choose $(\widehat{r},\,\widehat{x})$ values corresponding to the effective cutoffs $\tilde{\Lambda}_2,\tilde{\Lambda}_3\gtrsim 500\,\text{GeV}$. Note that the effective cutoff scale $\tilde{\Lambda}_j=\Lambda/\sqrt{f_{\Phi,j}}$ is not exactly the mass scale of an underlying new particle (as the dimensionless coupling $f_{\Phi,j}$ could be larger than one and is usually less than about 4π). One example is the model of Higgs-gravity interactions in Sec. 2.2 with dimension-6 operators (2.21)-(2.22). From the viewpoint of effective theory, the

[12] Depending on the luminosity, there could be $\mathcal{O}(10\%)$ statistical uncertainty in the last M_{hh} bin at $30\,\text{ab}^{-1}$. But the statistical uncertainties in other bins are much smaller.

Table 2: Selected events in different M_{hh} bins for the SM signal and backgrounds at the pp (100TeV) collider with an integrated luminosity of $3\,\text{ab}^{-1}$.

M_{hh} bins (GeV)	[300, 500]	[500, 700]	[700, 900]	[900, 1100]
$h(b\bar{b})h(\gamma\gamma)$ (SM)	200	170	52.5	11.1
$b\bar{b}h(\gamma\gamma)$	67.1	31.9	15.8	3.81
$Z(b\bar{b})h(\gamma\gamma)$	11.2	2.77	0.46	0.04
$t\bar{t}h(\gamma\gamma)$	97.5	15.9	3.22	0.58
$t\bar{t}\gamma\gamma$	5.41	1.1	0.24	0.0
$t\bar{t}\gamma$	13.9	1.09	0.16	0.05
$b\bar{b}\gamma\gamma$	188	23.7	5.25	0.32
$b\bar{b}j\gamma$	107	11.8	3.44	1.32
$jj\gamma\gamma$	30.3	2.58	0.82	0.24
Total Backgrounds	521	90.8	29.4	6.37

major issue is to make sure that the energy scale is within the perturbative unitarity bound, so that the perturbative analysis is valid. In Fig. 2, the plots (b)-(c) show that for the effective cutoff $\tilde{\Lambda}_2 \gtrsim 500\,\text{GeV}$, the unitarity bounds on the scattering energy are well above 1 TeV. This justifies our perturbative analysis of signal events with dihiggs invariant-mass $M_{hh} \lesssim 1.1\,\text{TeV}$.

For each benchmark, we first analyze the sensitivities in different M_{hh} bins as defined in (4.39). For a given set of $(\widehat{r},\,\widehat{x})$, the 68% C.L. contour is defined as follows,

$$\frac{\Delta S_i(\widehat{r},\,\widehat{x})}{\sqrt{B_i + S_i(\widehat{r},\,\widehat{x})}} \;=\; 1\,, \tag{4.42}$$

where signal S_i and background B_i in Table 2 denote the numbers of selected events in a given bin $M_{hh}^{(i)}$, and $\Delta S_i(\widehat{r},\,\widehat{x}) = |S_i(\widehat{r}+\delta\widehat{r},\,\widehat{x}+\delta\widehat{x}) - S_i(\widehat{r},\,\widehat{x})|$. The dependence of signal on the parameters $(\widehat{r},\,\widehat{x})$ is determined by the numerical fits in Eq. (4.40). Around the origin of $(\widehat{r},\,\widehat{x})$, it is well approximated by the linear expansion, $S_i \simeq c_i + a_i\delta\widehat{r} + b_i\delta\widehat{x}$. It means that the signal is only sensitive to the combination $a_i\delta\widehat{r} + b_i\delta\widehat{x}$, but not the perpendicular direction $b_i\delta\widehat{r} - a_i\delta\widehat{x}$. We call the later as "degenerate direction", along which the signal remains constant nearby the origin. Using the fit (4.38), we further derive the sensitivity contour with inclusive data.

$$\frac{\displaystyle\sum_i \Delta S_i(\widehat{r},\,\widehat{x})}{\sqrt{\displaystyle\sum_i [B_i + S_i(\widehat{r},\,\widehat{x})]}} \;=\; 1\,. \tag{4.43}$$

Finally, to fully utilize the information of different M_{hh} bins, we can derive the combined contour at 68% C.L.,

$$\sum_i \left(\frac{\Delta S_i}{\sqrt{B_i + S_i}}\right)^2 \;=\; 1\,, \tag{4.44}$$

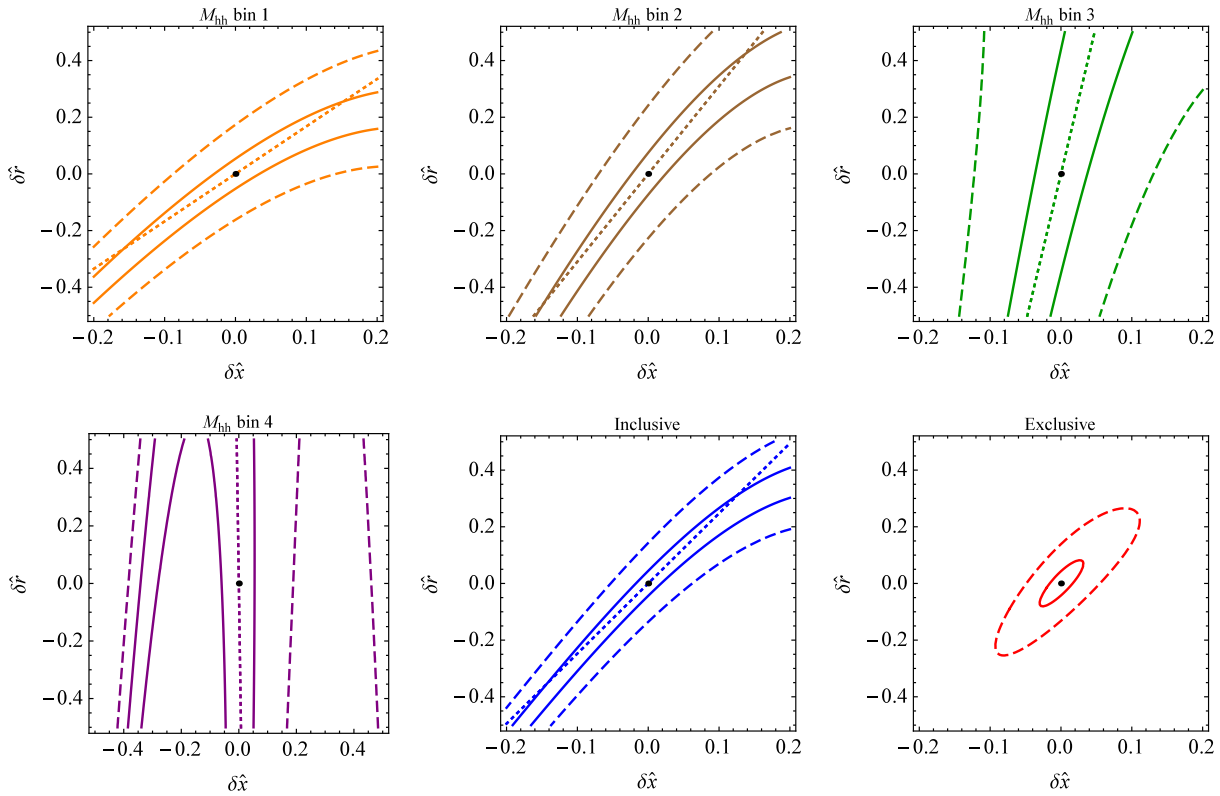

Figure 9: Sensitivity to $\delta\widehat{r} - \delta\widehat{x}$ around Benchmark A, $(\widehat{r}, \widehat{x}) = (0, 0)$. In each plot, the dashed (solid) curve depicts 68% C.L. contour with $3\,\text{ab}^{-1}$ ($30\,\text{ab}^{-1}$) integrated luminosity, and the dotted line denotes the degenerate direction around the origin. Plots (a)-(d) present the results for each M_{hh} bin. Plots (e) and (f) show the inclusive sensitivity (4.43) and exclusive sensitivity (4.44), respectively.

which we will call "exclusive" sensitivity. This is stronger than the "inclusive" sensitivity (4.43) which only uses the total rates.

In Fig. 9, we analyze the sensitivity for Benchmark A, which corresponds to taking the central values $(\widehat{r}, \widehat{x}) = (0, 0)$ as in the SM. We present the 68% C.L. contours for each M_{hh} bin in the plots (a)-(d). Then, we show the inclusive sensitivity contour (4.43) in plot-(e), and the exclusive sensitivity contour (4.44) in plot-(f). For each plot, the dashed (solid) curve depicts 68% C.L. contour with $3\,\text{ab}^{-1}$ ($30\,\text{ab}^{-1}$) integrated luminosity, while the dotted line shows the degenerate direction around the origin. The slope of dotted line varies for different bins of M_{hh}. It is clear that higher M_{hh} bins are more sensitive to $\widehat{x}$, as also noted before [27, 25]. However, the final sensitivity of a given bin also depends on the number of selected events in this bin. Due to suppression in the tail region of M_{hh} distribution, events number in the highest bin (purple) could be quite small. This is the case with $3\,\text{ab}^{-1}$ data in Fig. 9(d), where the sensitivity to $\widehat{x}$ is much lower than that in other bins. So, the inclusive sensitivity is mainly determined by the first two bins. For $30\,\text{ab}^{-1}$ data, there are enough events in the last bin to probe $\widehat{x}$ with a good accuracy. Impressively, since

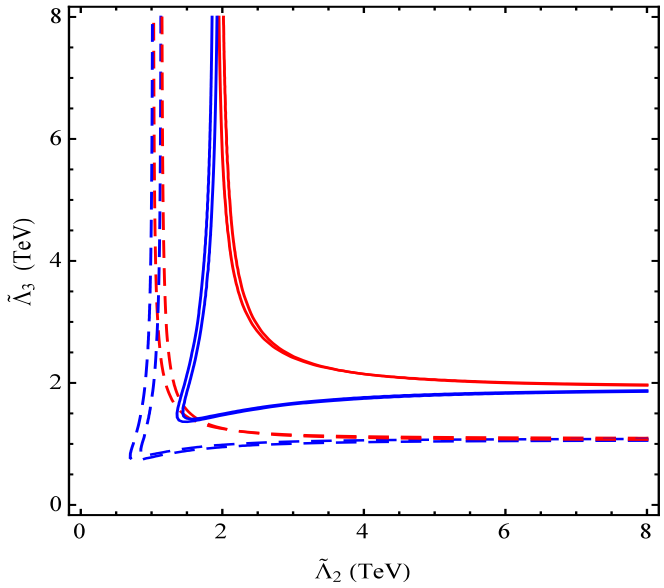

Figure 10: Exclusive sensitivity contours (68% C.L.) in $\tilde{\Lambda}_2 - \tilde{\Lambda}_3$ plane for Benchmark A at the pp(100TeV) collider with an integrated luminosity of $3\,\text{ab}^{-1}$ (dashed curves) and $30\,\text{ab}^{-1}$ (solid curves). The two red and blue contours correspond to $x_2x_3 > 0$ and $x_2x_3 < 0$, respectively. The region on the right-hand-side of each contour (and above it) is allowed.

various bins are sensitive to different combinations of $\widehat{r}$ and $\widehat{x}$, the exclusive analysis (4.44) makes a big improvement of the sensitivity, as shown in Fig. 9(f). Note that the exclusive analysis does not improve much of the sensitivity for each parameter alone, but helps to break the degenerate direction in the 2-dimensional plane. This demonstrates the important role played by the derivative cubic Higgs coupling $\widehat{x}$ in the dihiggs production. It means that gluon fusion production could probe both $(\widehat{r}, \widehat{x})$ to a good accuracy. This is a new point. For comparison, we derive the sensitivity to each parameter alone by fixing the other parameter to its SM value. We find that the exclusive sensitivity to $\delta\widehat{r}$ is about 13% (4.2%), and that to $\delta\widehat{x}$ is about 5% (1.6%), for the $3\,\text{ab}^{-1}$ ($30\,\text{ab}^{-1}$) integrated luminosity.

In Fig. 10, we present the exclusive sensitivity contours (68% C.L.) in $\tilde{\Lambda}_2 - \tilde{\Lambda}_3$ plane for Benchmark A at the pp(100TeV) collider with an integrated luminosity of $3\,\text{ab}^{-1}$ (dashed curves) and $30\,\text{ab}^{-1}$ (solid curves). The region on the right-hand-side of each contour (and above it) is allowed. The cases of $x_2x_3 > 0$ ($\widehat{x}\,\widehat{r} < 0$) and $x_2x_3 < 0$ ($\widehat{x}\,\widehat{r} > 0$) are shown by the two red and blue contours, respectively. For each contour, the asymptotically flat or vertical behavior gives the sensitivity to one operator (when the other is absent), which can be read from the intersection of 68% C.L. sensitivity contour in Fig. 9(f) with each axis. The sensitivities of probing the two operators are comparable, $\tilde{\Lambda}_2, \tilde{\Lambda}_3 \gtrsim 1\,\text{TeV}$ with $3\,\text{ab}^{-1}$, and $\tilde{\Lambda}_2, \tilde{\Lambda}_3 \gtrsim 2\,\text{TeV}$ with $30\,\text{ab}^{-1}$. For the blue contours, the cusps correspond to the end points of ellipse long axis in Fig. 9(f). These cusp regions give the weakest 2d sensitivities, $\tilde{\Lambda}_2, \tilde{\Lambda}_3 \gtrsim 0.75\,\text{TeV}$ for $3\,\text{ab}^{-1}$ data, and $\tilde{\Lambda}_2, \tilde{\Lambda}_3 \gtrsim 1.4\,\text{TeV}$ for $30\,\text{ab}^{-1}$ data.

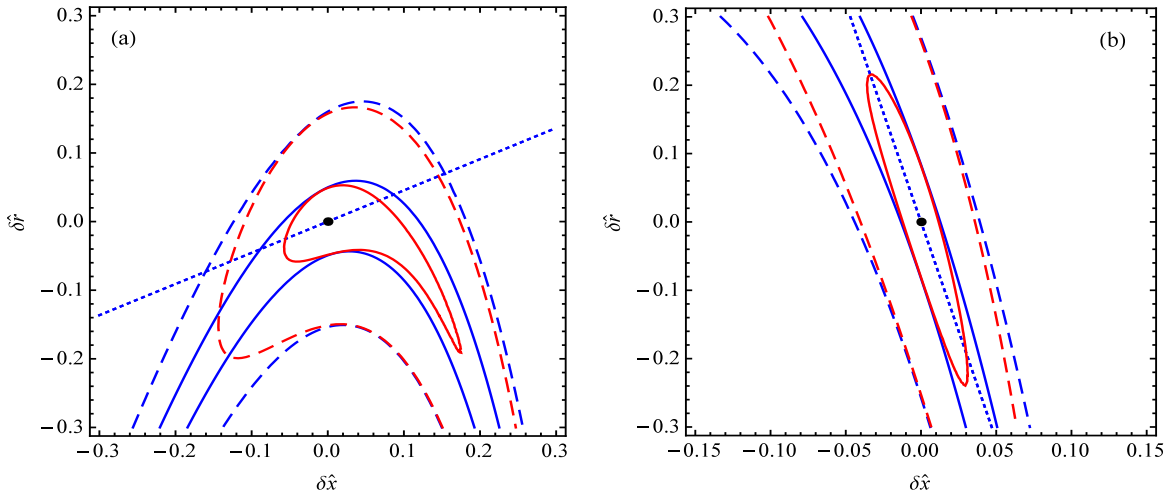

Figure 11: Sensitivity contours in $\delta\widehat{r} - \delta\widehat{x}$ plane for Benchmark B_1 with $(\widehat{r},\, \widehat{x}) = (0,\, 0.2)$ as shown in plot-(a), and for Benchmark B_2 with $(\widehat{r},\, \widehat{x}) = (0,\, 0.5)$ as shown in plot-(b). In each plot, the dashed (solid) curve depicts 68% C.L. contour with $3\,\mathrm{ab}^{-1}$ ($30\,\mathrm{ab}^{-1}$) integrated luminosity, and the dotted line denotes the degenerate direction around the origin. The blue and red contours depict the inclusive sensitivity (4.43) and exclusive sensitivity (4.44), respectively.

For the red contours, the 2d sensitivity is always stronger.

In Fig. 11, we present the inclusive sensitivity (4.43) and exclusive sensitivity (4.44) for Benchmark B_1 [plot-(a)] and Benchmark B_2 [plot-(b)] by blue and red contours, respectively. The dashed (solid) curve depicts 68% C.L. contour with $3\,\mathrm{ab}^{-1}$ ($30\,\mathrm{ab}^{-1}$) integrated luminosity, and the dotted line denotes the degenerate direction around the origin. The Higgs gravitational interaction predicts $\widehat{r} = 0$ and $\widehat{x} > 0$. As shown in plots (a) and (b), the sensitivity contours, including slope of the degenerate direction, strongly depend on the explicit value of $\widehat{x}$. Fig. 12 demonstrates the sensitivities for Benchmark C_1 [plot-(a)] and Benchmark C_2 [plot-(b)], where $\widehat{x} = 0$ and two nonzero $\widehat{r}$ values take opposite signs. We find that their shape and sensitivity range are quite similar to that of Benchmark A (the SM case). This is expected given the fact that the dihiggs total cross section and invariant-mass (M_{hh}) distribution are much more sensitive to $\widehat{x}$ than $\widehat{r}$.

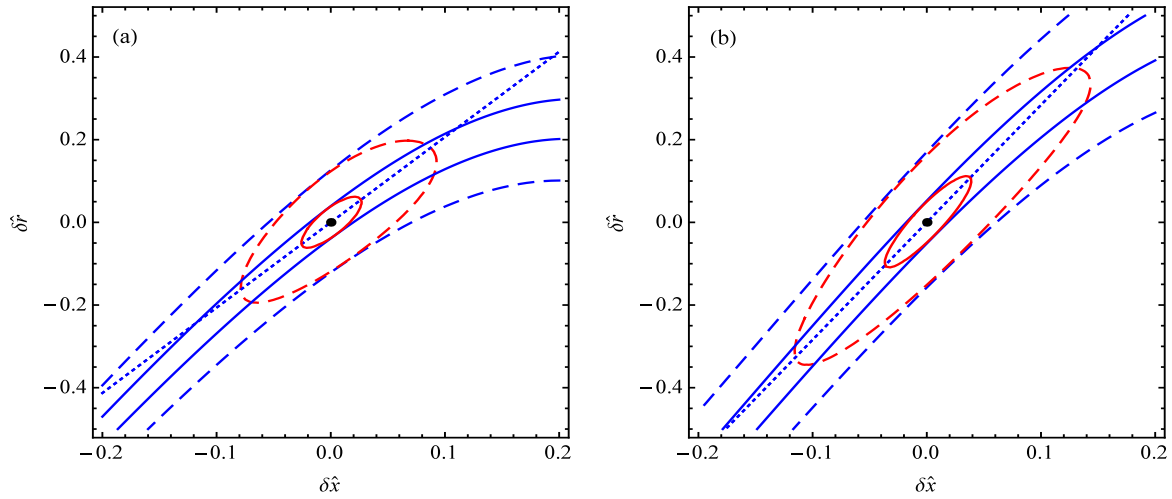

Figure 12: Sensitivity contours in $\delta\widehat{r} - \delta\widehat{x}$ plane for Benchmark C_1 with $(\widehat{r},\, \widehat{x}) = (-0.5,\, 0)$ as shown in plot-(a), and for Benchmark C_2 with $(\widehat{r},\, \widehat{x}) = (0.5,\, 0)$ as shown in plot-(b). In each plot, the dashed (solid) curve depicts 68% C.L. contour with $3\,\mathrm{ab}^{-1}$ ($30\,\mathrm{ab}^{-1}$) integrated luminosity, and the dotted line denotes the degenerate direction around the origin. The blue and red contours depict the inclusive sensitivity (4.43) and exclusive sensitivity (4.44), respectively.

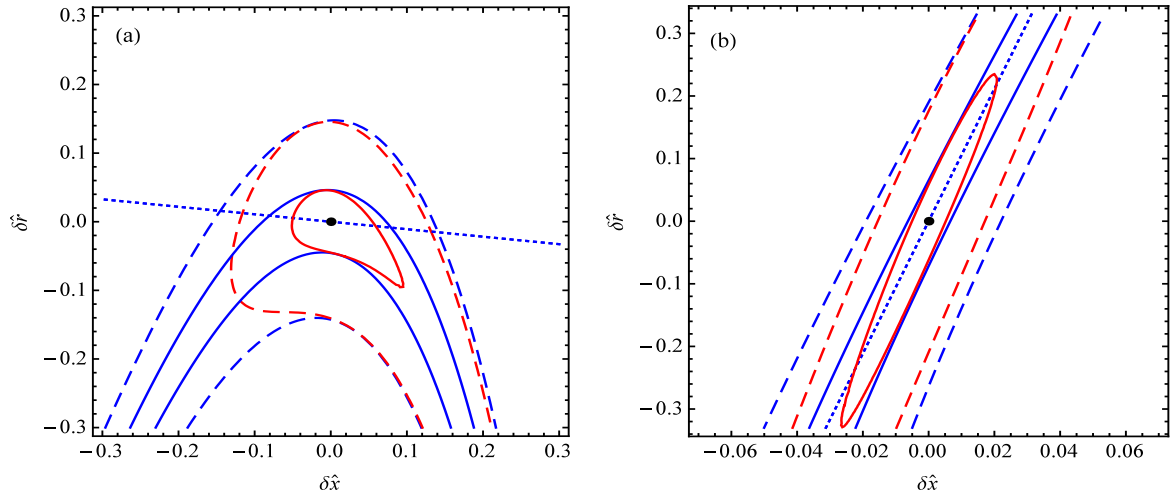

Figure 13: Sensitivity contours in $\delta\widehat{r} - \delta\widehat{x}$ plane for Benchmark D_1 with $(\widehat{r},\, \widehat{x}) = (-0.5,\, 0.2)$ as shown in plot-(a), and for Benchmark D_2 with $(\widehat{r},\, \widehat{x}) = (0.5,\, 0.5)$ as shown in plot-(b). In each plot, the dashed (solid) curve depicts 68% C.L. contour with $3\,\mathrm{ab}^{-1}$ ($30\,\mathrm{ab}^{-1}$) integrated luminosity, and the dotted line denotes the degenerate direction around the origin. The blue and red contours depict the inclusive sensitivity (4.43) and exclusive sensitivity (4.44), respectively.

In Fig. 13, we present the inclusive sensitivity (4.43) and exclusive sensitivity (4.44) for Benchmark D_1 [plot-(a)] and Benchmark D_2 [plot-(b)] to illustrate the features for $(\widehat{r},\, \widehat{x})$ both nonzero. Benchmark D_1 represents the case that the signals in the first two bins of M_{hh} are quite insensitive to $\delta\widehat{x}$ at the linear order, and the shape of the 68% sensitivity contour is mainly determined

by quadratic terms. Although the last two bins still have strong dependence on $\widehat{x}$, the inclusive sensitivity is determined by the first two bins (due to their large rates) with parabola-like shape. The exclusive sensitivity is largely improved, especially with $30\,\text{ab}^{-1}$ data. Fig. 13(b) presents the sensitivity contours (68% C.L.) for Benchmark D_2, where all M_{hh} bins have strong dependence on $\widehat{x}$. The sensitivity to $\widehat{x}$ is significantly enhanced as compared to other Benchmarks.[13] Since the sensitivity has little change among different bins, the 68% contour is only slightly improved by the exclusive analysis (4.44).

In summary, the qualitative feature of sensitivity contour in the $\delta\widehat{r} - \delta\widehat{x}$ plane can vary significantly for different benchmarks. In some cases (such as Benchmarks A, B_1, C_1, C_2, and D_1), the exclusive analysis of different M_{hh} bins makes big improvements. In particular, it can break the possible degenerate direction around the origin, and impose much stronger constraints on the 2d parameter space even with the dihiggs production measurement alone. For some other cases (such as Benchmarks B_2 and D_2), the parameter-dependence of signals appears quite similar in different bins. Thus, both the exclusive and inclusive analyses give comparable sensitivity.

5. Conclusions

Despite the LHC Higgs discovery, the Higgs boson self-interaction is fully untested so far. It is the key ingredient of Higgs potential, and plays vital roles for electroweak symmetry breaking, vacuum stability, electroweak phase transition, and Higgs inflation. This is a most likely place to encode new physics beyond the standard model (SM).

In this work, we studied the probe of cubic Higgs interactions via dihiggs production at hadron colliders. We parametrized the new physics of Higgs self-interactions in terms of model-independent dimension-6 effective operators in section 2. We take the nonminimal Higgs-gravity interaction as an explicit example to motivate such effective operators. The contributions of the two dimension-6 operators (2.16) to cubic Higgs couplings have different kinematic structures as shown in Eq. (2.10). They give different kinematic distributions in various dihiggs production channels due to the different energy-dependence. This is demonstrated in Figs. 5–7 of section 3. We also analyzed the weak boson scattering and $t\bar{t}$ scattering at high energies, and derived perturbative unitarity constraints on the parameter space in Fig. 2. Among the three channels of dihiggs production, top-pair associated production and vector boson fusion (VBF) production are more sensitive to the energy-enhancement in high energy collisions, though their cross sections are generally smaller than the gluon fusion production (Fig. 4).

In section 4, we performed systematical Monte Carlo analysis of dihiggs production $gg \to hh$

[13] Note that the plot range of $\delta\widehat{x}$ in Fig. 13(b) is much smaller than that in Fig. 13(a).

in the decay channel $hh \to b\bar{b}\gamma\gamma$ by using Delphes 3 fast detector simulations. We computed both signals and full SM backgrounds at the $pp\,(100\text{TeV})$ collider with a $3\,\text{ab}^{-1}$ integrated luminosity, as summarized in Table 1 and Fig. 8. This channel shows a good potential of discovering cubic Higgs couplings in $pp\,(100\text{TeV})$ collisions. Our derived significance is in main agreement with the literature [25], while a difference from [51] appears due to the different assumptions about detector performance. We further studied the probe of new physics effects in the $\widehat{r}-\widehat{x}$ parameter space with full simulations. Since different bins of the dihiggs invariant-mass M_{hh} exhibit distinctive kinematical features, we used them to discriminate the two dimension-6 operators. We did an exclusive analysis to incorporate such kinematical information and obtained a big improvement of sensitivity. We further identified four kinds of representative benchmarks (4.41) for the parameter space of cubic Higgs coupling, which have qualitatively different features. For each benchmark, we studied the sensitivity to the 2d parameter space of $(\widehat{r},\,\widehat{x})$, via both the inclusive analysis (4.43) and exclusive analysis (4.44). For comparison, we used two sample integrated luminosities ($3\,\text{ab}^{-1}$ and $30\,\text{ab}^{-1}$) of the $pp\,(100\text{TeV})$ collider. For Benchmark A (SM case), the exclusive analysis breaks the degeneracy in the 2d plane and makes it possible to probe both $(\widehat{r},\,\widehat{x})$ to a good accuracy by the dihiggs measurement alone. This is demonstrated in Fig. 9–10. For one-parameter analysis, we found that with a $3\,\text{ab}^{-1}$ ($30\,\text{ab}^{-1}$) integrated luminosity, the exclusive sensitivity to $\widehat{r}$ and $\widehat{x}$ are about 13% (4.2%) and 5% (1.6%), respectively. Fig. 11 presented Benchmarks B_1 and B_2 with $\widehat{r}=0$ and $\widehat{x}>0$, as motivated by nonminimal Higgs-gravity interaction. We found that the sensitivity contours strongly depend on the size of $\widehat{x}$. Fig. 12 analyzed Benchmarks C_1 and C_2 with $\widehat{x}=0$ and different values of $\widehat{r}$. As expected, the dependence on the change of $\widehat{r}$ is pretty weak. For general regions with $(\widehat{r},\,\widehat{x})$ both nonzero, we found the sensitivity contours to be qualitatively different from the SM case of $(\widehat{r},\,\widehat{x})=(0,\,0)$, as shown in Fig. 13(a)-(b) for Benchmarks D_1 and D_2. In the case where the parameter-dependence of signals in different bins is similar, such as Benchmark D_2 in Fig. 13(b), the improvement of the exclusive analysis over the inclusive analysis becomes rather modest.

A. Redundancy of Dimension-6 Operators

In this appendix, we discuss the redundancy of dimension-6 operators in Eqs. (2.4) and (2.5). In the SM action, the Higgs sector contains the following terms,

$$S_{\text{sm}} \;\supset\; \int dx^4\Big[(D^\mu H)^\dagger(D_\mu H)+\mu^2 H^\dagger H-\lambda(H^\dagger H)^2-y_f\overline{L}Hf_R+\text{h.c.}\Big], \tag{A.45}$$

where $L=(f_L^u,\,f_L^d)^T$ denotes the $SU(2)_L$ doublet, and f_R the $SU(2)_L$ singlet. Then, we can derive EOM for the Higgs field, $(D^2H)^\dagger=\mu^2H^\dagger-2\lambda(H^\dagger H)H^\dagger-y_f\overline{L}f_R$, and its hermitian conjugate.

After integration by part, we can rewrite the operator $\mathcal{O}_{\Phi,2}$ as

$$\begin{aligned} 2\mathcal{O}_{\Phi,2} &= \partial^\mu(H^\dagger H)\partial_\mu(H^\dagger H) = -(H^\dagger H)\partial_\mu\partial^\mu(H^\dagger H) + (\text{total derivative}) \\ &= -(H^\dagger H)\left[2(D^\mu H)^\dagger(D_\mu H) + H^\dagger D^2 H + (D^2 H)^\dagger H\right] \\ &= -2\mathcal{O}_{\Phi,4} - 2\mu^2(H^\dagger H)^2 + 12\lambda\mathcal{O}_{\Phi,3} + \big(y_f\mathcal{O}_{\Phi,f} + \text{h.c.}\big), \end{aligned} \tag{A.46}$$

where $\partial^\mu(H^\dagger H) = D^\mu(H^\dagger H)$. In the above, we have neglected the total derivative term. We have also implemented the SM EOM in the last step, since we only keep operators up to dimension-6. With the relation (A.46), we may replace $\mathcal{O}_{\Phi,4}$ by other operators,

$$\begin{aligned} & \frac{1}{\Lambda^2}\Big[f_{\Phi,2}\mathcal{O}_{\Phi,2} + f_{\Phi,3}\mathcal{O}_{\Phi,3} + f_{\Phi,4}\mathcal{O}_{\Phi,4} + f_{\Phi,f}(\mathcal{O}_{\Phi,f} + \text{h.c.})\Big] \\ = \; & -\frac{\mu^2 f_{\Phi,4}}{\Lambda^2}(H^\dagger H)^2 + \frac{f_{\Phi,2} - f_{\Phi,4}}{\Lambda^2}\mathcal{O}_{\Phi,2} + \frac{f_{\Phi,3} + 6\lambda f_{\Phi,4}}{\Lambda^2}\mathcal{O}_{\Phi,3} + \left(\frac{2f_{\Phi,f} + y_f f_{\Phi,4}}{2\Lambda^2}\mathcal{O}_{\Phi,f} + \text{h.c.}\right) \\ \to \; & \frac{1}{v^2}\left\{(x_2 - x_4)\mathcal{O}_{\Phi,2} + \left(x_3 + x_4\frac{3M_h^2}{v^2}\right)\mathcal{O}_{\Phi,3} + \left[\left(x_f + \frac{y_f}{2}x_4\right)\mathcal{O}_{\Phi,f} + \text{h.c.}\right]\right\}. \end{aligned} \tag{A.47}$$

Note that this also shifts the quartic Higgs coupling in the original Higgs potential, but can be absorbed by a coupling redefinition, $\lambda \to \lambda - \mu^2 f_{\Phi,4}/\Lambda^2$. At the order of Λ^{-2}, the coupling λ in front of $f_{\Phi,4}$ can be replaced by the leading order relation $\lambda = M_h^2/2v^2$. Hence, for on-shell physical amplitudes, we can organize their dependence on $(f_{\Phi,2}, f_{\Phi,3}, f_{\Phi,4}, f_{\Phi,f})$ via the three combinations in (A.47).

B. Loop Functions for Triangle and Box Diagrams

For the analyses of Sec. 3–4, we need to compute cross sections of the dihiggs production via gluon fusion $g(p_a)g(p_b) \to h(p_c)h(p_d)$, which invoke loop functions of triangle and box diagrams [52]. The triangle loop function is given by

$$F_\triangle = \tau_f\left[1 + (1-\tau_f)f(\tau_f)\right], \tag{B.48a}$$

$$f(\tau_f) = \begin{cases} \arcsin^2\frac{1}{\sqrt{\tau_f}}, & \tau_f \geqslant 1, \\ -\frac{1}{4}\left[\log\frac{1+\sqrt{1-\tau_f}}{1-\sqrt{1-\tau_f}} - \mathrm{i}\pi\right]^2, & \tau_f < 1, \end{cases} \tag{B.48b}$$

where $\tau_f \equiv 4m_f^2/\hat{s}$, and $\hat{s}$ is the partonic center of mass energy. The box loop functions are defined as follows,

$$\begin{aligned} F_\Box &= \frac{1}{S^2}\left[4S + 8m_f^2 S C_{ab} - 2m_f^4 S(S+2\rho-8)(D_{abc}+D_{bac}+D_{acb})\right] \\ &\quad + m_f^2(2\rho-8)\left[\overline{T}(C_{ac}+C_{bd}) + \overline{U}(C_{bc}+C_{ad}) - m_f^2(TU-\rho^2)D_{acb}\right], \end{aligned} \tag{B.49a}$$

$$\begin{aligned} G_\Box &= \frac{1}{S(TU-\rho^2)}\Big\{ m_f^2(T^2+\rho^2-8T)\left[SC_{ab} + \overline{T}(C_{ac}+C_{bd}) - m_f^2 STD_{bac}\right] \\ &\quad + m_f^2(U^2+\rho^2-8U)\left[SC_{ab} + \overline{U}(C_{bc}+C_{ad}) - m_f^2 SUD_{abc}\right] \\ &\quad - m_f^2(T^2+U^2-2\rho^2)(T+U-8)C_{cd} \\ &\quad - 2m_f^4(T+U-8)(TU-\rho^2)(D_{abc}+D_{bac}+D_{acb})\Big\}, \end{aligned} \tag{B.49b}$$

where $\rho = M_h^2/m_f^2$, $S = \hat{s}/m_f^2$, $T = \hat{t}/m_f^2$, $U = \hat{u}/m_f^2$, $\overline{T} = T-\rho$ and $\overline{U} = U-\rho$. The two scalar integrals are given by

$$C_{ij} = \int \frac{d^4q}{\mathrm{i}\pi^2} \frac{1}{(q^2-m_f^2)\left[(q+p_i)^2-m_f^2\right]\left[(q+p_i+p_j)^2-m_f^2\right]}, \tag{B.50a}$$

$$D_{ijk} = \int \frac{d^4q}{\mathrm{i}\pi^2} \frac{1}{(q^2-m_f^2)\left[(q+p_i)^2-m_f^2\right]\left[(q+p_i+p_j)^2-m_f^2\right]\left[(q+p_i+p_j+p_k)^2-m_f^2\right]}. \tag{B.50b}$$

In the low energy limit $\hat{s} \ll m_f^2$, the loop functions behave as

$$F_\triangle = \frac{2}{3} + \mathcal{O}\left(\frac{\hat{s}}{m_f^2}\right), \qquad F_\Box = -\frac{2}{3} + \mathcal{O}\left(\frac{\hat{s}}{m_f^2}\right), \qquad G_\Box = \mathcal{O}\left(\frac{\hat{s}}{m_f^2}\right). \tag{B.51}$$

In the high energy limit $m_f^2 \ll \hat{s}$, they take the asymptotical forms,

$$F_\triangle = -\frac{m_f^2}{\hat{s}}\left[\log\frac{m_f^2}{\hat{s}} + \mathrm{i}\pi\right]^2 + \mathcal{O}\left(\frac{m_f^2}{\hat{s}}\right), \qquad F_\Box = \mathcal{O}\left(\frac{m_f^2}{\hat{s}}\right), \qquad G_\Box = \mathcal{O}\left(\frac{m_f^2}{\hat{s}}\right). \tag{B.52}$$

Acknowledgments

We thank Nima Arkani-Hamed, Matthew Reece, and Matthew Strassler for discussions during the finalization of this work. We also thank Margarete Muhlleitner, Tilman Plehn and Michael Spira for correspondences and discussions. HJH was supported in part by National NSF of China, and the visiting grants of Harvard and IAS Princeton. JR was supported in part by the International Postdoctoral Exchange Fellowship Program of China. WY was supported in part by the Office of Science, Office of High Energy Physics, of the U.S. Department of Energy under contract DE-AC02-05CH11231.

References

[1] G. Aad *et al.* [ATLAS Collaboration], Phys. Lett. B 716 (2012) 1 [arXiv:1207.7214 [hep-ex]]; S. Chatrchyan *et al.* [CMS Collaboration], Phys. Lett. B 716 (2012) 30 [arXiv:1207.7235 [hep-ex]].

[2] S. Weinberg, Phys. Rev. Lett. 19 (1967) 1264; A. Salam, in Elementary Particle Theory, Nobel Symposium No. 8, edited by N. Svartholm (Almqvist & Wiksells, Stockholm, 1968), p.367.

[3] F. Englert and R. Brout, Phys. Rev. Lett. 13 (1964) 321; P. W. Higgs, Phys. Rev. Lett. 13 (1964) 508; P. W. Higgs, Phys. Lett. 12 (1964) 132; G. S. Guralnik, C. R. Hagen, and T. Kibble, Phys. Rev. Lett. 13 (1965) 585; T. Kibble, Phys. Rev. 155 (1967) 1554.

[4] G. Aad *et al.* [ATLAS Collaboration], Eur. Phys. J. C (2015) arXiv:1507.04548 [hep-ex]; V. Khachatryan *et al.* [CMS Collaboration], Eur. Phys. J. C 75 (2015) 212 [arXiv:1412.8662].

[5] M. E. Peskin, arXiv:1312.4974 [hep-ph], in Snowmass 2013 Electronic Proceedings, Community Summer Study, Minneapolis, MN, USA, July 29–August 6, 2013; and references therein.

[6] W. Yao, arXiv:1308.6302 [hep-ph], in the Proceedings of the Snowmass Community Summer Study (CSS 2013), Snowmass on the Mississippi, July 29–August 6, 2013, Minneapolis, MN, USA.

[7] Snomass Higgs Working Group Report, arXiv:1310.8361 [hep-ex], Community Summer Study 2013: Snowmass on the Mississippi (CSS2013), July 29–August 6, 2013, Minneapolis, MN, USA; and references therein.

[8] F. Goertz, A. Papaefstathiou, L. L. Yang, J. Zurita, JHEP 1306 (2013) 016 [arXiv:1301.3492].

[9] J. Ellis, J. R. Espinosa, G. F. Giudice, A. Hoecker, and A. Riotto, Phys. Lett. B 679 (2009) 369 [arXiv:0906.0954 [hep-ph]]; D. Buttazzo, G. Degrassi, P. P. Giardino, G. F. Giudice, F. Sala, A. Salvio, and A. Strumia, JHEP 1312 (2013) 089 [arXiv:1307.3536 [hep-ph]]; M. Fairbairn and R. Hogan, Phys. Rev. Lett. 112 (2014) 201801 [arXiv:1403.6786 [hep-ph]]; A. Kobakhidze and A. Spencer-Smith, arXiv:1404.4709 [hep-ph]; and references therein.

[10] V. Branchina and E. Messina, Phys. Rev. Lett. 111 (2013) 241801 [arXiv:1307.5193 [hep-ph]]; V. Branchina, E. Messina and M. Sher, Phys. Rev. D 91 (2015) 013003 [arXiv:1408.5302 [hep-ph]].

[11] For a review, M. Trodden, Rev. Mod. Phys. 71 (1999) 1463 [hep-ph/9803479]; and references therein.

[12] For a review, F. Bezrukov, Class. Quant. Grav. 30 (2013) 214001 [arXiv:1307.0708]; and references therein.

[13] W. Buchmuller and D. Wyler, Nucl. Phys. B 268 (1986) 621.

[14] A. Djouadi, W. Kilian, M. Muhlleitner, and P. M. Zerwas, Eur. Phys. J. C 10 (1999) 45 [hep-ph/9904287]; U. Baur, T. Plehn and D. L. Rainwater, Phys. Rev. D 68 (2003) 033001 [hep-ph/0304015]; Phys. Rev. D 69 (2004) 053004 [hep-ph/0310056].

[15] For a review, A. Djouadi, Phys. Rept. 457 (2008) 1 [arXiv:hep-ph/0503172]; and references therein.

[16] T. Plehn and M. Rauch, Phys. Rev. D **72** (2005) 053008 [hep-ph/0507321]; and references therein.

[17] J. Baglio, A. Djouadi, R. Grober, M. M. Mhlleitner, J. Quevillon and M. Spira, JHEP 1304 (2013) 151 [arXiv:1212.5581 [hep-ph]]; R. Frederix, S. Frixione, V. Hirschi, F. Maltoni, O. Mattelaer, P. Torrielli, E. Vryonidou and M. Zaro, Phys. Lett. B 732 (2014) 142 [arXiv:1401.7340 [hep-ph]].

[18] E.g., V. Barger, L. L. Everett, C. B. Jackson, A. D. Peterson and G. Shaughnessy, Phys. Rev. D 90 (2014) 095006 [arXiv:1408.2525 [hep-ph]]. A. J. Barr, M. J. Dolan, C. Englert, D. E. Ferreira de Lima and M. Spannowsky, JHEP 1502 (2015) 016 [arXiv:1412.7154 [hep-ph]].

[19] The ATLAS Collaboration, ATL-PHYS-PUB-2014-019, October 21, 2014.

[20] U. Baur, T. Plehn and D. L. Rainwater, Phys. Rev. Lett. 89 (2002) 151801 [hep-ph/0206024]; M. J. Dolan, C. Englert and M. Spannowsky, JHEP 1210 (2012) 112 [arXiv:1206.5001 [hep-ph]]; A. Papaefstathiou, L. L. Yang and J. Zurita, Phys. Rev. D 87 (2013) 011301 [arXiv:1209.1489 [hep-ph]]; A. J. Barr, M. J. Dolan, C. Englert and M. Spannowsky, Phys. Lett. B 728 (2014) 308 [arXiv:1309.6318 [hep-ph]]; D. E. Ferreira de Lima, A. Papaefstathiou and M. Spannowsky, JHEP 1408 (2014) 030 [arXiv:1404.7139 [hep-ph]]; C. Englert, F. Krauss, M. Spannowsky and J. Thompson, Phys. Lett. B 743 (2015) 93 [arXiv:1409.8074 [hep-ph]]; and references therein.

[21] Q. Li, Z. Li, Q. S. Yan, X. Zhao, arXiv:1503.07611 [hep-ph].

[22] A. Papaefstatihiou, arXiv:1504.04621 [hep-ph].

[23] C. Englert, F. Krauss, M. Spannowsky and J. Thompson, Phys. Lett. B 743 (2015) 93 [arXiv:1409.8074 [hep-ph]]; T. Liu and H. Zhang, arXiv:1410.1855 [hep-ph].

[24] M. J. Dolan, C. Englert, N. Greiner and M. Spannowsky, Phys. Rev. Lett. 112 (2014) 101802 [arXiv:1310.1084 [hep-ph]].

[25] A. Azatov, R. Contino, G. Panico and M. Son, arXiv:1502.00539 [hep-ph].

[26] F. Goertz, A. Papaefstathiou, L. L. Yang and J. Zurita, arXiv:1410.3471 [hep-ph].

[27] C. R. Chen and I. Low, Phys. Rev. D 90 (2014) 013018 [arXiv:1405.7040 [hep-ph]].

[28] C. T. Lu, J. Chang, K. Cheung, and J. S. Lee, arXiv:1505.00957 [hep-ph].

[29] S. Weinberg, Phys. Rev. Lett. 43 (1979) 1566.

[30] T. Corbett, O. J. P. Eboli, J. Gonzalez-Fraile and M. C. Gonzalez-Garcia, Phys. Rev. D 87, 015022 (2013) [arXiv:1211.4580 [hep-ph]]; and references therein.

[31] J. Ellis, V. Sanz and T. You, JHEP 1503 (2015) 157 [arXiv:1410.7703 [hep-ph]].

[32] E.g., M. Ruan *et al.,* arXiv:1411.5606 [hep-ex], "Higgs measurement at e^+e^- circular colliders", presentation at 37th International Conference on High Energy Physics (ICHEP-2014), July 2-9, 2014, Valencia, Spain.

[33] N. Craig, M. Farina, M. McCullough, M. Perelstein, JHEP 1503 (2015) 146 [arXiv:1411.0676].

[34] M. McCullough, Phys. Rev. D 90 (2014) 015001 [arXiv:1312.3322 [hep-ph]].

[35] R. Brock, M. E. Peskin, K. Agashe, M. Artuso, J. Campbell, S. Dawson, R. Erbacher and C. Gerber *et al.*, arXiv:1401.6081 [hep-ex].

[36] N. A. Chernikov and E. A. Tagirov, Annales Poincare Phys. Theor. A 9 (1968) 109;
C. G. Callan, Jr., S. R. Coleman and R. Jackiw, Annals Phys. 59 (1970) 42.

[37] M. Atkins and X. Calmet, Phys. Rev. Lett. 110 (2013) 051301 [arXiv:1211.0281 [hep-ph]].

[38] J. Ren, Z. Z. Xianyu, H. J. He, JCAP 1406 (2014) 032 [arXiv:1404.4627 [gr-qc]];
Z. Z. Xianyu, J. Ren, H. J. He, Phys. Rev. D 88 (2013) 096013 [arXiv:1305.0251].

[39] J. Ren and H. J. He, JCAP 1503 (2015) 052 [arXiv:1410.6436].

[40] For a review, H. J. He, Y. P. Kuang and C. P. Yuan, DESY-97-056 [arXiv:hep-ph/9704276]; and references therein.

[41] D. A. Dicus and H. J. He, Phys. Rev. D 71 (2005) 093009 [hep-ph/0409131]; Phys. Rev. Lett. 94 (2005) 221802 [hep-ph/0502178].

[42] J. Alwall, M. Herquet, F. Maltoni, O. Mattelaer and T. Stelzer, JHEP 1106 (2011) 128 [arXiv:1106.0522 [hep-ph]].

[43] S. Dawson, S. Dittmaier and M. Spira, Phys. Rev. D **58**, 115012 (1998) [hep-ph/9805244]; J. Grigo, J. Ho, K. Melnikov and M. Steinhauser, Nucl. Phys. B 875 (2013) 1 [arXiv:1305.7340 [hep-ph]]; R. Frederix, S. Frixione, V. Hirschi, F. Maltoni, O. Mattelaer, P. Torrielli, E. Vryonidou and M. Zaro, Phys. Lett. B 732 (2014) 142 [arXiv:1401.7340 [hep-ph]]; F. Maltoni, E. Vryonidou and M. Zaro, JHEP 1411 (2014) 079 [arXiv:1408.6542 [hep-ph]]; D. de Florian and J. Mazzitelli, Phys. Lett. B 724 (2013) 306 [arXiv:1305.5206 [hep-ph]]; Phys. Rev. Lett. 111 (2013) 201801 [arXiv:1309.6594 [hep-ph]]; J. Grigo, K. Melnikov and M. Steinhauser, Nucl. Phys. B 888 (2014) 17 [arXiv:1408.2422 [hep-ph]].

[44] R. Grober, M. Muhlleitner, M. Spira and J. Streicher, arXiv:1504.06577 [hep-ph].

[45] E. Conte, B. Fuks and G. Serret, Comput. Phys. Commun. 184 (2013) 222 [arXiv:1206.1599 [hep-ph]].

[46] D. A. Dicus, C. Kao, W. W. Repko, arXiv:1504.02334 [hep-ph].

[47] [ATLAS Collaboration], ATL-PHYS-PUB-2013-007 and arXiv:1307.7292 [hep-ex].

[48] T. Sjostrand, S. Mrenna and P. Z. Skands, JHEP 0605, 026 (2006) [hep-ph/0603175].

[49] J. de Favereau *et al.,* [DELPHES 3 Collaboration], JHEP 1402 (2014) 057 [arXiv:1307.6346].

[50] ATLAS Collaboration, "Performance assumptions for an upgraded ATLAS detector at a High-Luminosity LHC," ATL-PHYS-PUB-2013-004 (2013).

[51] A. J. Barr, M. J. Dolan, C. Englert, D. E. Ferreira de Lima and M. Spannowsky, JHEP 1502 (2015) 016 [arXiv:1412.7154 [hep-ph]].

[52] T. Plehn, M. Spira, and P. M. Zerwas, Nucl. Phys. B 479 (1996) 46 [Erratum, B 531 (1998) 655] [hep-ph/9603205].